Evaluating the capabilities of the Pierre Auger Observatory to search for axion-like particles

Masterarbeit
zur Erlangung des akademischen Grades
Master of Science
(M.Sc.)

vorgelegt an der

Department Physik

vorgelegt von

Chiara Jane Papior

am 17.08.2022

Betreuer und erster Gutachter:	Prof. Dr. Markus Risse
Zweiter Gutachter:	Prof. Dr. Markus Cristinziani

Abstract. In this thesis the possibilities to search for axions and axion-like particles via the Pierre Auger Observatory are evaluated. Axions are postulated elementary particles which have not been detected in experiments yet. If they do exist, they might be able to provide solutions to several problems which are left unanswered by the Standard Model of particle physics. Axions could potentially interact with photons in external magnetic fields which leads to the assumption that they could possibly be produced in stars, supernovae, binary neutron star mergers and other events. The goal is to answer the question if there are sources from which axions could possibly be detected and to give a guideline on which sources to investigate in detail in future searches. An optimistic guideline is provided for future axion searches via the Pierre Auger Observatory predicting that it is worthwhile to analyse signals from sources similar to GW170817 up to luminosity distances at the gigaparsec scale with the current setup of the Observatory.

Contents

1 Introduction

1.1 The beginning of astrophysics

For thousands of years we as humans have been looking up into the sky with fascination. Ancient cultures have legends and myths about the creation of the universe and the movement of stars and planets visible to us. The Milky Way has been seen as a river by ancient Egyptians who believed the sun-god Ra sailed across every day [1]. Some of the aboriginal peoples of Australia saw a river in the sky as well with nebulae representing campfires, lit by their ancestors, or light from the spirits of the dead [2]. Besides the Milky Way and shining stars the planets of our solar system were noticed by ancient civilisations as well [2], [1]. It took centuries of studying these planets to understand the movements visible on the night sky. One of the most famous early systems of describing the dynamics of planets in the solar system was proposed by Pythagoras around 500 BC. It described the earth and other celestial bodies as spherical objects moving on circular paths around a central fire. This model included the earth, moon and sun as well as the five planets visible by the bare eye. The whole system was surrounded by a sphere of fire called Olympus. The sun was assumed to made of a glass-like substance reflecting the light from Olympus or the central fire. This model also included a counterearth, never directly visible but a possible explanation for eclipses of the moon. Another model was proposed by Anaxagoras. He proposed that the sun was a 'red hot mas' illuminating the moon which he assumed to be earth-like and not shining by its own light. But even though parts of these models were correct and by coincidence provided an explanation for eclipses, they still assumed the earth to be flat, supported by air in the center of the universe. The heliocentric view was proposed at around 310-250 BC by Aristarchus of Samos. He assumed that the earth moved around on a perfect circle around the sun. This theory and similar approaches were rejected and the view of the geocentric view persisted. In the 16th century the heliocentric view was proposed again by Copernicus. At the end of the 16th century and the beginning of the 17th century progress was made by Tycho Brahe and Galileo Galilei in the field of astronomy by adding to the plausibility of the heliocentric model by observations of the phases of Venus and the satellites of Jupiter through a refracting telescope. But even though the heliocentric model provided a much better explanations for the observations of orbital movements, it was not generally accepted. The observations of Brahe were put to use again by Kepler. Instead of spherical movements of planets, he proposed elliptical orbits. He also established the Kepler's laws of planetary motion we know today. This model gained acceptance during the 17th century and when Newtons theory of gravitation and his three laws of motion offered an explanation for the elliptical movement of planets the geocentric model became obsolete. These laws still form the basis of Newtonian mechanics today. With the refracting telescopes and later the reflecting telescope constructed by Newton, observations of many more distant stars became possible. However, until the late 19th century it was believed that astronomy only existed to explain the motion of stars. In the 19th century the methods of 'spectroscopy, photometry and photography' were discovered and offered new possibilities [1]. Theoretical physics also made advances during this time and the idea of the sun being a gaseous body instead of a liquid or even solid one became widely accepted. The new founded branch of astrophysics gained popularity

fast. With that, large refracting telescopes were constructed especially in America surpassing one another in size. The cataloguing of star spectra led to a major step in the comprehension of stellar evolution [1]. Einsteins special and general theory of relativity contributed to astrophysical research as well. In the early 20th century cosmic radiation was discovered and extensive air showers produced by cosmic rays interacting with earth's atmosphere where measured for the first time [3]. Pierre Auger was one of the first physicists researching in this field. He can be considered the 'discoverer of giant airshowers' which are generated by the interaction of cosmic rays with particles in the earth's atmosphere [4].

1.2 Particle physics and the Standard Model

To understand the phenomenon of air showers we need to understand the basis of particle physics first. The Standard Model of Elementary Particles (SM) offers an explanation for a lot of phenomena observable in the realm of particle physics. It contains twelve elementary particles as well as their interactions via the fundamental forces. The particles of the SM are called fermions, they have a half-integer spin and are grouped into quarks and leptons. The six leptons are split up into particles where 3 of them are charged with an electric charge and three of them being neutral particles. The charged particles are the widely known electron as well as the muon and tauon which can be differentiated by their mass. For each of these charged particles there is a corresponding neutrino which are neutral and are considered massless in the SM. The 6 different types of leptons are also referred to as flavours. There are 6 quarks as well which are divided into 3 up-type- and 3 down-type-quarks called up, charm and top and down, strange and bottom, respectively. These types are known as quark-flavours. Up-type-quarks have an electrical charge of 2/3 while down-type quarks have one of $-1/3$. Quarks also have an additional colour charge, which can either be red, green or blue. Quarks are differentiated by their masses as well with the up-quark being the lightest and the top-quark being the heaviest.

Additionally to these particles, the SM allows for anti-particles as well. Anti-particles have the same mass as their corresponding particle but the electric charge and colour charge are reversed.

The SM does not only describe the existence of particles and anti-particles but also interactions between them. These fundamental interactions are called electromagnetic, strong, weak and gravitational. The SM only covers the first three of these which seems counterintuitive as the gravitational force is the one most noticeable in our everyday life but on a atomic scale the other forces are much stronger than the gravitational force. The three interactions present in the SM are associated by the force carriers, also called gauge bosons. The electromagnetic and strong interaction described by so called quantum-electrodynamics (QED) and quantum-chromodynamics (QCD), respectively. They are mediated by the photon and gluon, respectively, which are both massless and have no electrical charge. Photon has also no colour-charge while gluons have a combination of two colour-charges. Particles with an electric charge interact via the electromagnetic force and particles with colour charge interact via the strong interaction. Gluons bind quarks together to composite particles forming a colour singlet where for each colour there is a corresponding anticolour or where all colours are present in the same quantity resulting in a colour-

singlet. The weak force has more than one mediator, the $W^{\pm}$- and Z-boson where the W-bosons have an electric charge of ± 1 while the Z-boson is electrically neutral. They also do not have a colour charge but in contrast to the other gauge bosons they are massive. All fermions can interact via the weak interaction. The weak and electromagnetic interaction are also referred to as the combined electroweak interactions which are described by quantum-flavour dynamics (QFD). There is the additional Higgs-boson in the SM, it is not a gauge boson and therefore not a force-carrier but it is necessary for the breaking of the electroweak symmetry which then results in the W- and Z-bosons being massive. An overview of the SM particles as well as the interactions can be seen in Fig. 1.

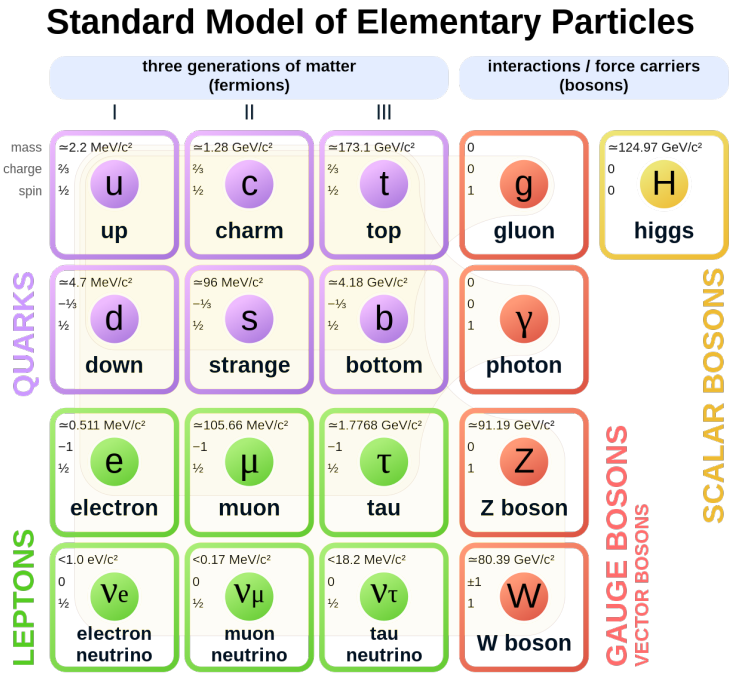

Figure 1: Standard Model of Particle Physics [5].

It is important to notice that the weak interaction is the only interaction that allows for flavour changing interactions and it is the only interaction allowing the breaking of the parity symmetry (P-symmetry) and the charge parity symmetry (CP-symmetry). The conservation of P-symmetry in electromagnetic and strong interactions means that interactions proceed in the same way even if the sign of one or all spacial coordinates are flipped. Similarly if an interaction cannot be distinguished from another interaction with a sign-change in one or all spacial coordinates and an exchange from particles to anti-particles or vice versa, the CP-symmetry is conserved.

Besides mass and electric charge, particles can also be classified by their spin which can be described as an intrinsic angular momentum. Bosons have an integer spin while fermions have a half-integer spin.

From the elementary particles described above, composite particles called hadrons can be formed by the strong interaction. Hadrons consisting of 2 quarks are called mesons, they have an integer spin and are therefore classified as bosons. Composite

particles containing 3 quarks are called baryons, they have a half-integer spin and are therefore considered fermions.

Mathematically the SM can be described as a quantum field theory where particles as well as force carriers are classified as quantum fields. All of the interactions between such fields but also the motion of particles themselves can be expressed by a Lagrangian density often called Lagrangian for short.

Theoretically the SM can also be viewed as a combination of symmetries. The three forces described by the SM each contribute a local symmetry. There is the $SU(2) \times U(1)$ electroweak symmetry and the $SU(3)$ colour-symmetry associated with the strong interaction. The combined $SU(3) \times SU(2) \times U(1)$ symmetry is the theoretical foundation of the SM [6]. Besides these local symmetries there are several global symmetries such as the conservation of the total number of baryons and the conservation of energy and momentum.

The SM provides explanations for interactions between particles and particle decays and makes accurate predictions in elementary particle physics below the energy of the Fermi scale of weak interaction also referred to as electroweak scale which lies at about 246 GeV [7]. But even though the SM describes fundamental particles and their interactions, it can not be considered a full theory. As mentioned above, gravitational forces are not acknowledged at all and there are other phenomena that cannot be explained by only the SM. There is no candidate for the dark matter in our universe, no explanation for dark energy and none of the SM particles are able to solve the strong CP-problem. Theories beyond the SM are necessary to fully understand and explain our universe. But before some of these problems are discussed in more detail, we will move back to cosmic radiation.

1.3 Cosmic radiation and air showers

First direct evidence for cosmic radiation was discovered in the early 20th century by Victor Hess who made measurements on the radiation in the atmosphere. Ionizing radiation had been measured in the atmosphere and Hess was searching for a source by taking an electroscope on a balloon and taking measurements over 5000 meters above sea level. He found that the rate of ionisation was three times as high up in the atmosphere which led to the conclusion that the radiation must be coming from above and not from the rocks of the earth as it was assumed until then [8]. Pierre Auger did research in the same field and concluded that the measurable electromagnetic radiation resulted from exotic particles colliding with atmospheric nuclei. This results in cascades of secondary particles containing electromagnetic radiation which are referred to as air showers [9].

In air shower experiments several new particles, amongst them muons, pions and kaons, were first discovered. The first antiparticle, the positron, was first seen in air showers as well. The energies of the incoming particles span over a range of 11 magnitudes, from 1 GeV up to 10^8 TeV and in the beginning of the 20th century cosmic rays were the only possible method to study particles of such high energies and even today the energies of air shower still exceed the ones achievable in accelerator experiments [9]. The number of cosmic rays detected at different energies, which is referred to as flux, spans over 30 orders of magnitude while roughly following $d\Phi/dE \propto E^{\alpha}$ where $d\Phi/dE$ describes the flux per energy, E refers to the energy and

$\alpha \simeq -3$ is referred to as the spectral index. The energy spectrum of cosmic rays can be seen in Fig. 2.

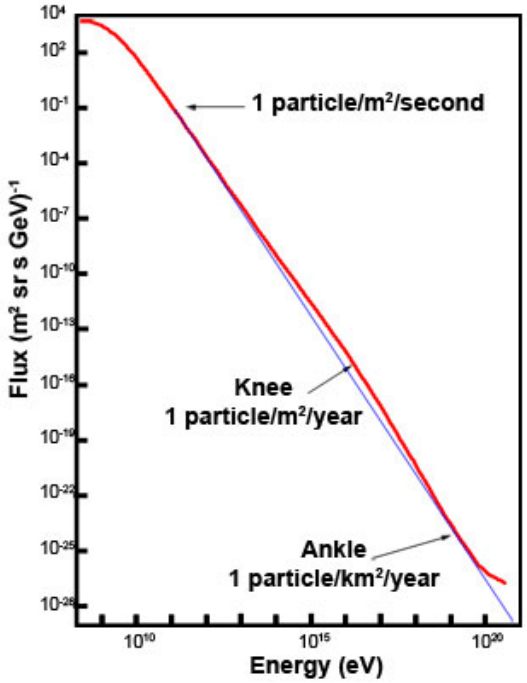

Figure 2: The Cosmic Ray energy spectrum[10].

The flux reaches from several thousand particles per square meter and second to less than one particle per square kilometer and year. Due to this decrease of flux, direct measurements of primary particles via satellites and balloons become more complicated and expensive for high energy particles. Therefore not much data is available from direct measurements above energies in the PeV-range. But with ground-based detectors, searching for the secondary particles of air showers, measurements are possible even at high energies. With increasing energies, less and less particles reach the earth and large detectors are needed. There are several experiments and observatories utilizing direct and indirect methods to search for cosmic rays and air showers but the focus here will be on the Pierre Auger Observatory which is currently the largest cosmic ray observatory. It was named after Pierre Auger who was one of the first researchers in the field of cosmic radiation.

1.4 The Pierre Auger Observatory

The Pierre Auger Observatory is located in Argentina near the city of Malargüe and makes ground-based measurements of extensive air showers. It covers an area of 3000 km^2 and is currently the largest and most precise detector for ultra-high-energy air showers [11],[12]. It is based on two different methods of detection. The first measurement technique is a surface detector consisting of 1660 water Cherenkov detectors. The particle detection is based on Cherenkov radiation that occurs when particles travel through water faster than the velocity of light in the water. This Cherenkov light can be detected by photomultiplier tubes. One cosmic ray event can

produce Cherenkov light in several tanks due to the width of an air shower and due to minimal differences in detection time the trajectory of the initial particle can be reconstructed [13].

The second element of the Pierre Auger Observatory are 27 Fluorescence detectors at four different locations. Charged particles in an air shower interact with nitrogen in the earth's atmosphere which results in ultraviolet fluorescence light. With this part of the detector the development of an air shower can be tracked and if it occurs in an area where it is visible from two or more of the locations, the trajectory can be measured very precisely [13].

With measurements from both detection methods a lot of information about the cosmic ray event can be extracted such as the shower depth and the total energy of the shower and therefore of the primary particle as well as the particles trajectory.

1.4.1 Neutral particles in cosmic rays

Neutral particles like photons play an especially important role for researchers. Charged particles propagating through galactic and intergalactic medium towards earth from distant sources are deflected by magnetic fields of different strengths which are present everywhere. For neutral particles this is not the case, they propagate in a straight line directly from their origin. Reconstructing their trajectory can provide information on the source of those particles. Therefore a differentiation between showers induced by different kinds of particles is necessary. Such a distinction can be provided by the Pierre Auger Observatory as showers induced by different particles have distinct particle content and develop differently in the atmosphere [12].

Both neutral particles and charged particles contribute greatly to multimessenger astronomy as they are created by different processes and propagate in different ways and therefore contribute information about the universe, its content and its evolution.

2 Axions and axion-like particles

As mentioned in chapter 1.2 there are several phenomena observed in nature that cannot be explained with our current theory, the SM. New theories and physics beyond the SM are necessary to understand and explain the universe around us. Some of these phenomena can be explained by assuming the existence of new particles.

2.1 The strong CP-problem

The first problem that will be discussed here is the strong CP-problem. Above it was stated that the only interaction allowing for the breaking of the CP-symmetry is the weak interaction, in strong- and electromagnetic interaction this symmetry appears to be conserved. The first CP-violating interactions was observed in the 1960s which led to the inclusion of this phenomenon in the theory. Different interactions conserve different symmetries and on first glance it is reasonable to assume that there is a CP-symmetry present in the strong but not in the weak interaction. But by including a CP-breaking term in the Lagrangian of the weak sector of the SM, a CP-breaking term occurs in the QCD sector as well [14]. To illustrate the CP problem we will focus on a simplified QCD model with only one quark [15]. The Lagrangian can be written as

$$\mathcal{L} = -\frac{1}{4} G_{\mu\nu} G^{\mu\nu} - \frac{\theta \alpha_s}{8\pi} G_{\mu\nu} \tilde{G}^{\mu\nu} + \bar{\psi} \left(i\gamma^\mu D_\mu - m e^{i\theta' \gamma_5} \right) \psi \tag{1}$$

with the first and third term being the kinetic terms of the quark field and gauge field which contain the gluon field strength tensor $G_{\mu\nu} = \partial_\mu \mathcal{A}_\nu - \partial_\nu \mathcal{A}_\mu \pm i\sqrt{4\pi\alpha_s}[\mathcal{A}_\mu, \mathcal{A}_\nu]$ of the gluon field $\mathcal{A}_\mu$ and its dual $\tilde{G}_{\mu\nu} = \frac{1}{2}\epsilon_{\mu\nu\rho\lambda} G_{\rho\lambda}$ [16],[15]. These terms conserve the CP-symmetry. The terms relevant for the problem at hand are the second and fourth term containing the θ-parameter and the chiral phase θ' of the fermion mass respectively. If θ and θ' are non-zero, the CP-symmetry is broken. By redefining the quark fields $\psi' = e^{i\alpha\gamma_5/2}\psi$ and $\bar{\psi}' = \bar{\psi} e^{-i\alpha\gamma_5/2}$ both the θ-term and the chiral phase are shifted to $\theta \to \theta + \alpha$ and $\theta' \to \theta' - \alpha$ [15]. By choosing $\alpha = \theta'$, the chiral phase is eliminated and the problem only remains in the θ-term where θ is replaced by $\bar{\theta} = \theta + \theta'$. It is possible that $\bar{\theta}$ is extremely small making CP-violating highly unlikely which could possibly explain why no CP-violating strong interaction has been observed yet. This, however, leads to a fine-tuning problem as there is no physical reason for a symmetry to be almost conserved [14]. Another solution to the problem is the introduction of an additional global $U(1)$ symmetry known as the Peccei-Quinn symmetry. The symmetry is chosen in such a way that it adds the term

$$\mathcal{L}_{\mathrm{PQ}} = \frac{\alpha_s}{8\pi} \frac{a}{f_a} G_{\mu\nu} \tilde{G}^{\mu\nu} \tag{2}$$

to the Lagrangian where a refers to the axion field, f_a to the symmetries energy scale and α_s to the strong coupling constant [17]. Here the fraction $\frac{a}{f_a}$ is chosen to equal $\bar{\theta}$ resulting in $\theta_{\mathrm{effective}} = 0$ and therefore canceling the problematic second term in equation (1) [18]. As the strong theory itself, the Peccei-Quinn symmetry is not exact but a pseudo symmetry which can be spontaneously broken at the scale f_a mentioned above. The spontaneous breaking of a symmetry generates an additional

particle, a Goldstone boson which in this case is called the Peccei-Quinn axion, QCD axion or simply axion [14]. As all Goldstone bosons the Peccei-Quinn axions are spinless and have an electric charge of zero. The term in equation (2) added to the Lagrangian allows for the interaction of axions with gluons as well as mesons, such as neutral pions, and through these interactions the axion acquires a mass which is related to the symmetry breaking scale via $m_a \approx \frac{m_\pi f_\pi}{f_a}$ where m_π and f_π refer to the mass and decay constant of the neutral pion respectively [19]. Additionally to these interactions there are more interaction terms that need to be added to the Lagrangian. This research is focused on the interaction between axions and photons and therefore other interactions will not be discussed in more detail. The axion-photon interaction term is given by

$$\mathcal{L}_{a\gamma} = \frac{g_{a\gamma} a}{4} F_{\mu\nu} \tilde{F}^{\mu\nu} \tag{3}$$

where $F_{\mu\nu} = \partial_\mu A_\nu - \partial_\nu A_\mu$ denotes the field strength tensor of the magnetic field A_μ and $\tilde{F}_{\mu\nu} = \frac{1}{2}\epsilon_{\mu\nu\rho\lambda} F_{\rho\lambda}$ refers to its dual [17]. As well as the axion mass the coupling strength $g_{a\gamma}$, sometimes also referred to as $g_{a\gamma\gamma}$, is related to the energy scale via $g_{a_\gamma} \approx \frac{\alpha}{2\pi f_a}$ [19]. Therefore the axion mass and coupling strength of the Peccei-Quinn axion are related to each other. The given Lagrangian allows for the axion to decay into two photons. For allowed values for the energy scale and therefore the coupling strength, the lifetime of the Peccei-Quin axion is larger than the age of the universe, therefore it can be considered stable for all practical purposes [17]. Another possible axion-photon interaction is the conversion from axions into photons or vice versa in the presence of an external magnetic field with a field component transversal to the direction of propagation of the converting particle [17], [7]. A Feynman diagram of the Primakoff conversion from an axion into a photon is shown in Fig. 3 but both

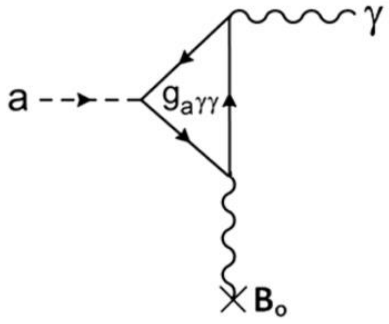

Figure 3: Feynman diagram of the Primakoff conversion of an axion into a photon within an external magnetic field [21].

the conversion from axions to photons and from photons to axions are referred to as Primakoff conversion. These interactions are only possible in an external magnetic field due to the fact that axions are spinless while photons have a spin one. It is worth noting that the oscillation of photons into axions leads to a change in the polarisation state of a photon beam as only photons with a polarisation parallel to the magnetic field convert into axions depleting this polarisation component [7].

2.1.1 Axion-like particles

When discussing the interactions of axions and photons it is important to mention axion-like particles (ALPs). As the initially introduced QCD axion, ALPs are Goldstone bosons resulting from the spontaneous breaking of symmetries similar to the Peccei-Quinn symmetry at a high energy scale [17]. They are predicted by different theories such as supersymmetric models, string theories and Kaluza-Klein theories. Peccei-Quinn axions and ALPs have a similar Lagrangian structure, they are both spinless and have an electric charge of zero. While the mass and the coupling strength to photons are related for the Peccei-Quinn axion, there is no such relation for ALPs, their mass and coupling strength are independent parameters [7].

The focus in the following research will be mostly on ALPs due to the larger axion mass-coupling strength parameter space but most of the discussion does not exclude Peccei-Quinn axions. To avoid confusion, both ALPs as well as Peccei-Quinn axions will be referred to as axions from now on. If one or the other is meant specifically they will be referred to as Peccei-Quinn axions or ALPs, respectively.

2.1.2 Production of axions

As axions interact with several different particles of the SM there are different production mechanisms but as mentioned above, the focus will be on the production via the Primakoff conversion. This process can happen when photons are present in an external magnetic field such as in the interior of stars, where there is a large quantity of thermal photons and electrostatic fields of electrons or nuclei [17]. The number of photons is correlated to the temperature and therefore the production rate is increased in hotter stars. In contrast the production rate decreases with increasing density in the stellar interior due to high plasma frequencies resulting in non-zero effective photon masses [22] which decrease the probability of photons converting into axions. Therefore the axion production is most prominent in stars with a high temperature and low density, which is the case for Helium burning stars, but axions may be produced in other stars as well. Hydrogen and helium burning stars such as our sun can be found on the main sequence and on the horizontal branch (HB) of the Hertzsprung-Russell diagram respectively. The Hertzsprung-Russel diagram shows the relation between the luminosity of a star and its effective temperature providing a guideline for the classification of evolutionary stages of stars which can be seen in Fig. 4.

Stars in the horizontal branch are on a stellar evolution stage right after the Red Giant Branch (RGB) containing stars of low to intermediate mass with a helium core. If the Primakoff effect takes place in HB stars, their evolution is speed up compared to the ones in the RGB which is a possible explanation for the observed reduction of the ratio R of the number of stars in the HB to the number of stars in the RGB. The measurement of R or also called the R-factor leads to the strongest bound on the axion-photon coupling strength [17].

A conversion process of thermal photons into axion can not only occur in helium- and hydrogen burning stars but in events like supernovae, active galactic nuclei or neutron star mergers as well as in other high energetic events where photons and strong magnetic fields are present. Axions emitted from such high energetic events may have been converted from high energetic photons and therefore have high ener-

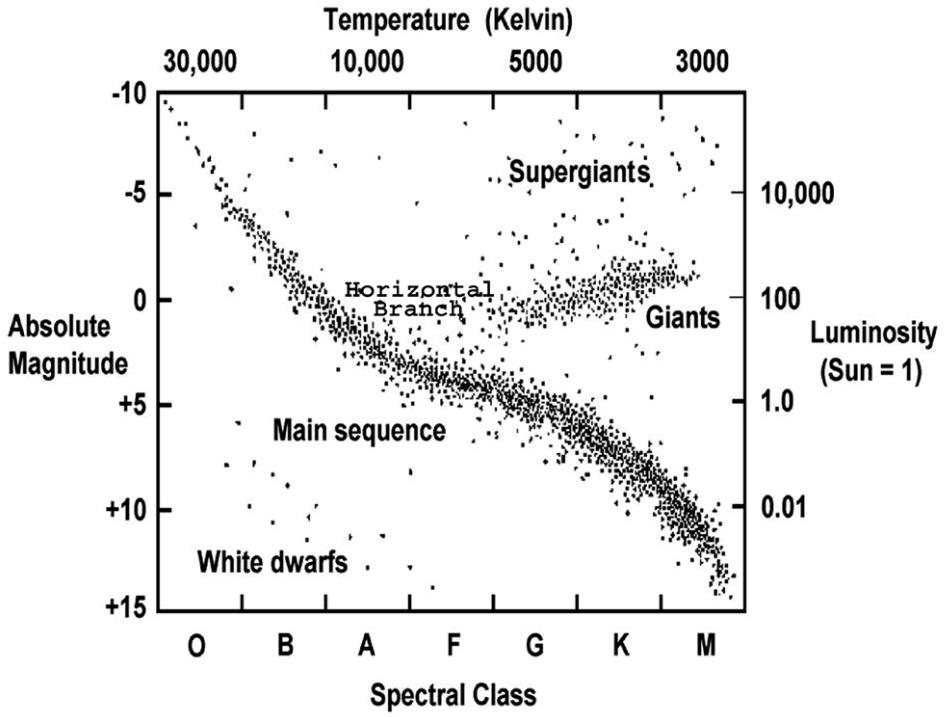

Figure 4: Hertzsprung-Russel diagram [23].

gies themselves making them relativistic. Such axions could possibly contribute to hot dark matter.

There are two additional production mechanisms of axions which could have occurred in the early stages of universe. Due to a population of thermal photons in the early universe and magnetic fields, thermal axions could have been produced at this time. Due to the high energy density of the universe at that point, these axions would be relativistic as well. And as they do have a low coupling strength, they would barely loose energy over time and they would still be relativistic today. Therefore they could contribute to a hot dark matter population as well [17].

Additionally to the production via Primakoff conversion there is another axion production mechanism worth mentioning here. This mechanism is provided by the initial theory itself and has the potential to provide a solution to one of the biggest questions left open by current theories. In the early universe temperatures were extremely high, they exceeded the breaking scale of the PQ-symmetry or similar symmetries responsible for ALPs. During the expansion and therefore cooling of the universe at one point the temperature crossed the breaking scale of the symmetry leading to a spontaneous symmetry breaking. To understand how this process works, we have to take a look at the Higgs-field ϕ and its potential and differentiate between scenarios where the spontaneous symmetry breaking occurred before and after the inflation period of the universe. In both scenarios the phase of the Higgs fields can be interpreted as the axion. Its potential has a single minimum at zero. In the pre-inflation scenario this potential transformed into one with a mexican-hat shape when the temperature of the universe decreased below the CP-symmetry breaking scale. The Higgs-field acquired a vacuum expectation value as the minimum of its potential

now had non-zero values and its phase took a random value in the valley of the potential. Therefore the PQ-symmetry, which can be seen as the rotational symmetry, was spontaneously broken. As the temperature decreased further beyond the QCD scale, QCD effects 'turned on' and provided the axion with its mass. The QCD-effects becoming relevant can be described as a tilting of the Higgs-field potential which caused the potential to have a definite minimum. The axion 'rolled' down towards the minimum of the potential and oscillated around it which corresponds to a coherent, non-relativistic axion population behaving like cold dark matter. Due to the misalignment between the random initial phase and the phase at the new minimum, this mechanism is known as vacuum realignment mechanism or axion misalignment mechanism [17].

The post-inflation scenario is slightly different. After the exponential expansion the universe became separated into several causally-disconnected areas or domains. In each of those domains the phase acquired a different random initial value. The axion still 'rolled' down towards the minimum of the potential after the temperature decreased below the QCD scale which led to patches of different axion densities in the universe that remain until today [17]. However, the average dark matter density can be calculated as the statistical average making this scenario highly predictable [24]. Unfortunately, another effect contributes to the cold dark matter population in the post-inflation scenario, it is referred to as the decay of topological effects. Topological effects may have occurred during the time in which the temperature fell below the PQ-symmetry breaking scale. The different areas or domains of the universe, which were causally disconnected, were separated by so called domain walls which topological cut off fields from the potential minimum. These domain walls stopped the axion from 'rolling' towards the global minimum which required a great amount of energy. As these domain walls were not stable, they shrunk and decayed later releasing the stored energy in the form of non-relativistic axions contributing to the cold dark matter density. The resulting axion density is much less predictable. Additionally the post-inflation scenario results in an axion population with a higher velocity dispersion compared to the axions produced in the pre-inflation scenario [17]. But as stated before, both scenarios produce non-relativistic axions possibly contributing to cold dark matter and therefore contributing to the solution of one of the open questions of the universe, the nature of the large amounts of dark matter that contribute to the overall energy-density of the universe.

2.2 The dark matter problem

Even though dark matter contributes the majority of the matter in our universe its nature is still unknown and as it is 'invisible' its existence was unknown for a long time as well.

The earliest evidence for dark matter came from the measurement of the rotational curves of galaxies. The planets in our solar system are stable on their orbits because of the balance of centrifugal and gravitational forces which results in an orbital speed $v \propto r^{-1/2}$ where r is the distance to the center of rotation. These calculations were made by Johannes Kepler based on the observations made by Tycho Brahe in the 16th century. Assuming that similarly to our solar system, the majority of a galaxy's mass was located in its center, as expected from the mass luminosity-relation, one

would expect a similar relation. However, the rotational speed of stars in the galaxies is almost constant even at great distances from the center [3]. The mass distribution in galaxies has to be significantly different to explain this observation, there needs to exist another mass component which does not emit light and is distributed over the galactic plane. The difference in expected and measured rotational curves was first observed by Fritz Zwicky in the 1930s who referred to this yet undetected matter as dark matter distributed in a so called dark matter halo around a galaxy [25]. This dark mass has still not been observed or visually detected in any direct way.

There is not only evidence for dark matter within the galaxies but in galaxy clusters as well. The mass of galaxy clusters can be estimated similarly to the mass of galaxies with a mass-luminosity relation but as with galaxies, an additional mass component is required to explain other observations. The velocity of galaxies within the cluster can be measured and it was discovered that these velocities exceed escape velocities which were calculated based on the visible mass of a cluster. Galaxy clusters would not hold together by gravitational force but gradually drift apart [25]. Dark matter existing in intergalactic space in galaxy clusters adds to the mass of the cluster, increases the gravitational force holding the cluster together and therefore potentially explains why galaxy clusters do not drift apart.

As mentioned above, dark matter is classified into hot dark matter and cold dark matter, referring to relativistic and non-relativistic particles. But only non-relativistic particles can solve the dark matter problem mentioned above as the particles required for the solutions of these problems need to be gravitationally bound to galaxies and clusters. Relativistic particles on the other hand have velocities exceeding the escape velocities and are therefore not gravitationally bound [3].

2.3 Dimming supernovae

Axions produced in supernovae might provide a solution to a different problem as well, the dimming of supernovae. The universe is usually assumed to be accelerating to explain why supernovae with a redshift of $0.3 \lesssim z \lesssim 1.7$ have a lower luminosity than expected [26]. From observations it is known that the universe is flat and only about 30% of the energy density in the universe is contributed by matter density, which itself is dominated by dark matter [26]. The remaining 70% of the energy density is compromised by a peculiar dark energy component. In current models describing an accelerating universe this dark energy component has a ratio of pressure over density or equation of state of $\frac{p}{\rho} \leq -\frac{2}{3}$ which is responsible for the accelerated expansion[26]. Possible options for this dark energy component are a small cosmological constant or a time-dependent quintessence energy but unfortunately, both of these options lead to a fine-tuning problem where extremely small parameters are required to fit the data [26]. There is, however, a different solution to the problem. For this model the universe is still assumed to be flat with a matter density of 30% [26]. Furthermore, it still contains a dark energy component contributing 70% to the energy density but the equation of state is changed to $\frac{p}{\rho} = -\frac{1}{3}$, meaning the expansion of the universe is not accelerated [26]. Additionally axions are introduced to the system. Photons emitted by supernovae propagate through intergalactic medium as well as galactic medium where magnetic fields of different strength and orientation are present causing the photons to convert into axions via Primakoff conversion during their propagation.

Similar to photons, axions are not deflected by magnetic fields and propagate mostly unhindered due to their low coupling strength but for the same reason they are not detected at earth [26]. This leads to a reduction in the detectable photon flux and therefore those distant supernovae appear to be fainter than they actually are. Hence, with axions the topic of cosmic acceleration may require some reconsideration.

2.4 Axions and cosmic rays

The last phenomenon that will be discussed here are cosmic rays, especially γ-rays, and their origin. Cosmic rays originate from a number of different sources, ranging from sources close by like our sun, over sources outside of our solar system to distant sources beyond the Milky Way such as active galactic nuclei. Such sources emit cosmic rays consisting of protons and atomic nuclei as well as photons with energies distributed over a wide spectrum. While electrically charged particles are deflected by magnetic fields during their propagation, photons propagate in a straight line from their origin towards earth. Traversing high-energy photons interact with the extragalactic background light (EBL) and cosmic microwave background (CMB) consisting of lower energy photons, producing electron-positron pairs ($\gamma + \gamma \rightarrow e^+ + e^-$). This reduces the photon flux.Therefore the cosmic microwave background (CMB) is opaque for ultra-high energy and high energy photons. There is, however, a tension between theory and experiment, as current EBL models predict a higher loss of photons than we detect with experiments measuring the spectra of active galactic nuclei (AGN). This over-prediction is noticeable as a hardening in the AGN spectra [17]. A lower EBL density or anomalously hard spectra are possible but unlikely solutions to the problem [24]. Axions are another possible explanation for these observations. Due to high magnetic fields at the source, emitted photons may be converted into axions via Primakoff-conversion, these axions then propagate mostly unhindered as their coupling strength is extremely low. The flux of axions is therefore not reduced. Axions are also not deflected by electromagnetic fields and propagate in a straight line just like photons. During their propagation they traverse magnetic fields in the intergalactic medium or galactic magnetic fields where they convert back into photons via Primakoff-conversion resulting in axion-photon oscillations similar to neutrino oscillations [17]. The existence of axions would not only provide an explanation for the tension between experiment and theory but would lead to and increase in the optical depth of the universe compared to calculations based on classical physics [17]. Axions are neutral messenger particles for which the CMB is transparent, they could therefore contribute greatly to multimessenger astronomy.

3 Searching for axions

There are several different methods to search for axions. They can be classified into direct and indirect searches. The indirect searches focus on effects and signatures that could possibly be caused by axions, the direct searches focus on the direct detection of axions in laboratories [17]. A few detection methods will be introduced here focusing on the ones based on interactions between axions and photons. This will be by no means a complete list of experiments searching for the existence of axions but rather a brief introduction to experimental searches.

3.1 Direct search for axions

Some of the different experimental methods aiming for the direct detection of axions via the axion-photon Primakoff conversion will be introduced here. Such experiments can provide bounds on the axion-photon coupling strength as well as the axion mass. It can be further distinguished between two methods, purely laboratory experiments producing and detecting axions and experiments aiming for the detection of naturally present axions.

3.1.1 Axion production in laboratories

Experiments purely based on axions produced in laboratories have the advantage of working without making assumptions about astrophysical processes. But they therefore cannot benefit from the predicted enormous flux of solar or dark matter axions. The 'light shining through wall' (LSW) experiments rely on bright sources of photons, e.g. lasers which send photons through a strong magnetic field perpendicular to the direction of propagation where Primakoff conversion is possible. The path is then blocked by an optical barrier stopping photons but not axions. After passing through the barrier the axions propagate through another magnetic field where a reconversion into photons is possible. Those photons can be detected. Two notable LSW experiments are the ALPs experiments at DESY and the OSQAR experiment at CERN [17].

With a similar setup polarisation experiments can be performed as well. The polarization component of the laser that is parallel to the magnetic field is affected by the photon-axion oscillation leading to a depletion, due to photons converting into axions, and a phase-delay, due to conversion from those axions back to photons [24]. The component perpendicular to the magnetic field is not altered. The strongest constraints in this field have been provided by the PVLAS experiment in Ferrara [17].

3.1.2 Search for solar axions

Axions could potentially be produced in the interior of the sun via the Primakoff process from photons in the presence of magnetic fields of electrons, protons or other ionised or partially ionised particles located in the plasma [24]. The axions produced this way would inherit energies of ≈ 3 keV from the photons and would therefore be relativistic. These axions could escape the gravitational potential well of the sun and would propagate unhindered through space. The axion flux could be rather large

which makes this detection method more sensitive than the laboratory-only method [17]. Axion Helioscopes which aim to detect solar axions work similarly to the LSW experiments. They are based on a vacuum filled telescope pointed towards the sun with a strong magnetic field of $B = 9.0$ T in the case of the CAST experiment at CERN which is transverse to the direction of propagation through the telescope. Axions that propagate through this magnetic field may convert into photons which have the same energy as the incoming axions making them X-ray photons which can be focused and detected [28].

Helioscopes are sensitive to a specific coupling strength but a wide range of axion masses [17]. At axion masses above $\approx 10^{-2}$ eV the coherence is lost and the experiment looses sensitivity. By filling the telescope with a buffer gas, the photon obtains an effective mass and if the axion mass matches the photon mass, coherence is restored. By increasing the gas pressure, the effective photon mass is increased which leads to an increase in sensitivity for higher axion masses [24]. Many groups working on helioscope experiments have joined into one single community called the IAXO collaboration which is working on a large scale helioscope as the successor of the CAST experiment at CERN [17].

Another method to detect solar axions is a time projection chamber. It consists of a large volume of magnetized gas with high photoabsorption [17]. Additionally to the magnetic field, an electric field is present. Axions are converted into photons due to the magnetic field and these photons interact with the gas producing free electrons. With the magnetic field, these are transported to one end of the detector where they produce a measurable signal. For this kind of detector the direction from which an axion is arriving is not important. Therefore the detection chamber does not need to be moved in order to point it at the sun which is advantageous in comparison to axion helioscopes [24]. For a conversion to happen there still needs to be a magnetic field component perpendicular to the direction of propagation, due to the rotation of the earth this perpendicular component varies leading to a daily modulation of the signal reaching us from the sun. This kind of experiment is sensitive to higher axion masses where measurements with the previously mentioned helioscopes starts to get more and more difficult.

3.1.3 Search for axions in the dark matter halo

Like solar axions, dark matter axions could be abundant around us assuming that dark matter is purely composed of axions. The velocity would stem from falling into the gravitational potential well of the galaxy which would result in non-relativistic axions [17]. Most of the experiments searching for axions in the dark matter halo are based on the Standard Halo Model, which is an idealised model where the halo is assumed to be self-gravitating with a Gaussian velocity distribution [29]. Therefore the axions are assumed to have a comparably low spread in velocity making them almost monochromatic [24]. Axion haloscopes aim to detect those axions via Primakoff conversion inside a microwave cavity located in a magnetic field. If an axion would convert into a photon in such a cavity and if the frequency of said photon matches the resonant frequency of the cavity a measurable signal would be produced. As the photons energy matches the one of the axion, the frequency of the converted photon would be highly dependent on the mass of the axion. In order to probe a large range

of possible axion masses, the resonant frequency of the cavity needs to be variable which is achieved by changing the geometry of the cavity. One of the first groups to work on axion haloscopes was the ADMX collaboration but recently there have been a few more groups working towards a similar goal, for example there are plans for a haloscope setup as part of the IAXO experiment [17].

Relatively high and low frequencies are both more complicated to realise in such a setup. Lower frequencies demand cavities with larger volume and therefore larger and more expensive magnets. Higher frequencies on the other hand require smaller cavities which result in fewer signals [24]. Therefore different methods are used for their detection for example a method utilizing a magnetized dish antenna consisting of a dielectric interface and a magnetic field parallel to this surface. A present axion field could lead to an emission of electromagnetic radiation perpendicular to the dielectric surface. With a curved surface, this radiation could be be concentrated into a small area where it can be detected. The advantage of this method is, that it is sensitive to all axion masses. There is however no resonance involved with this method, therefore large dielectric surfaces are needed. An alternative is a dielectric haloscope where several dielectric slabs are stacked in front of a mirror. Through constructive interference a present signal can be enhanced. By varying the distance between the dielectric slabs, the frequency range in which the signal is enhanced, can be modulated [17].

3.1.4 Search for axions in gamma rays

While the detection methods discussed above are more sensitive to low-energy axions, there are also ways to search for higher energetic axions emitted e.g. from supernovae. These axions could propagate towards earth and convert into photons during their propagation resulting in measurable γ-rays. No such event has been measured by the satellite experiments searching for such signals like the Solar Maximum Mission satellite [30]. The non-observation of such signals provides constraints on the coupling strength at low axion masses [17].

3.1.5 Searching for axions with the Pierre Auger Observatory

Another experiment that could be utilized for the search for axions in ultra-high energy cosmic rays (UHECRs) is the Pierre Auger Observatory mentioned in chapter 1.4 which is able to detect photons with energies above $\approx 10^{17}$ eV. The photons converted from axions collide with atmospheric particles which leads to electromagnetic cascades containing among others electrons, positrons and more photons. These secondary particles can be detected and their energies as well as direction of propagation can be reconstructed. As mentioned before it is also possible to distinguish photon induced showers from showers induced by other particles. The potential measurement of high-energetic photons without a close-by source would hint at the existence of axions. Other experiments based on the production of Cherenkov-light are Tibet ASγ [31] and HAWC [32] which are able to probe the energy range of 10 TeV$-$1 PeV. Measurements of photons in this energy range or the lack of such could be utilized to provide limits or constraints on axion parameters in the future.

3.2 Indirect search for axions

Besides the experimental constraints there are theoretical ones as well but even more important there are also hints for the existence of axions in specific parameter regions.

3.2.1 Effects on stellar evolution

Axions being produced in stellar interiors have effects on the stellar evolution due to the additional energy drain compared to the one predicted by SM physics. If this effect is only present in a specific stage during a stars existence, the corresponding area in the Hertzsprung-Russel diagram would contain fewer stars [17]. The axion production rate is especially high in Helium burning stars on the HB of the Hertzsprung-Russel diagram leading to an increased emission of energy. This results in more effective cooling and therefore speeds up the evolution of stars in this stage [17], [33]. Comparing the number of stars in this phase with the number of stars in the preceding phase, the RGB, provides an upper limit on the axion-photon coupling strength of $g_{a\gamma} < 0.66 \cdot 10^{-10}$ GeV^{-1} at 95% confidence level known as the HB bound [17]. The ratio of stars in the horizontal branch to the stars in the RGB is slightly smaller than expected hinting at a small coupling strength of $g_{a\gamma} = (0.29 \pm 0.18) \cdot 10^{-10}$ GeV^{-1} referred to as the HB-hint [17].

3.2.2 Effects on photon propagation

The propagation of axions from distant sources and their possible conversion into photons has been discussed in chapter 2.4. To explain the observed effects of a hardening of AGN spectra with axions, a axion mass in the range of $m_a \sim (10^{-10} - 10^{-7})$ eV and a coupling strength in the range of $g_{a\gamma} \sim (10^{-11} - 10^{-10})$ GeV^{-1} are necessary. This parameter region is referred to as T-hint [24] as it is relevant for energies in the TeV range.

3.2.3 White dwarf cooling hints

Another hint is provided by the mechanism of white-dwarf cooling [24]. White dwarves are relatively light, they are at the end of their lifetime and as their energy source is extinguished, there is no energy generated by fusion anymore. These stars cool via the emission of photons and neutrinos which is well-understood. There are however slight disagreements between theory and measurements regarding the white dwarf luminosity function which could be explained by an additional cooling mechanism possibly via axions. Additionally single pulsating white dwarves have been observed and it was discovered that their rate of change was larger than expected which could be explained by axion cooling as well. These measurements mostly hint at the existence of a non-zero coupling strength g_{ae} between axions and electrons but combined with the HB-hints a hinted region in the g_{ae}-$g_{a\gamma}$ parameter space can be extracted [17].

3.2.4 Dark matter bounds

The parameters of axionic dark matter can not only be constrained by experiments but theoretical considerations might provide bounds as well. For these hints, axions

produced by the symmetry breaking in the early universe are considered. Here we have to differentiate between the pre- and post-inflation scenario. For pre-inflation models the expected axion mass range is $m_a = (10^{-6} - 10^{-4})$ eV [17] but values as high as 10^{-3} eV and arbitrary low values are allowed as well. For post-inflation models the range is a little more confined. Different axion mass ranges of $m_a = (0.6 - 1.5) \cdot 10^{-4}$ eV and $m_a = (0.265 \pm 0.034) \cdot 10^{-4}$ eV have been proposed but more recent publications have considered higher axion masses of $m_a \gtrsim 5 \cdot 10^{-4}$ eV and $35 \cdot 10^{-4}$ eV depending on the specific axion models [17].

3.2.5 Black holes

Another constraint on the axion mass range can be deduced from a phenomenon called *blackhole superradiance*. For axions with very low masses, there are black holes with a radius of the same magnitude as the axions Compton wavelengths. Such black holes could loose angular momentum in the form of axions. The existence of black holes with large angular momentum therefore provides constraints on the mass of axions excluding the axion mass range $6 \cdot 10^{-13}$ eV $< m_a < 2 \cdot 10^{-11}$ eV [17].

These are only a few examples of theoretical constraints and hints on the axions parameter space but there are numerous more which will be not discussed here in detail.

3.3 Constraints on axion parameters

The experiments and some of the theoretical considerations mentioned above provide constraints on the mass and coupling strength of axions. The areas in the axion mass-coupling strength parameter space already probed by experiments can be seen in Fig. 5. The most recent constraints provided by Tibet ASγ and HAWC are not displayed in the diagrams yet but can be found in [27]. For axions in the sub-PeV range, these experiments have provided an upper limit on the coupling strength of $g_{a\gamma} < 2.1 \cdot 10^{-11}$ GeV^{-1} for axion masses $m_a \leq 10^{-7}$ eV at a 95% confidence level [27]. This limit is slightly lower than the one displayed in Fig. 5.

The hints mentioned above are displayed in Fig. 6 together with constraints by different experiments. It is noticeable that the most recent results by Tibet ASγ and HAWC partially but not fully exclude the hinted regions.

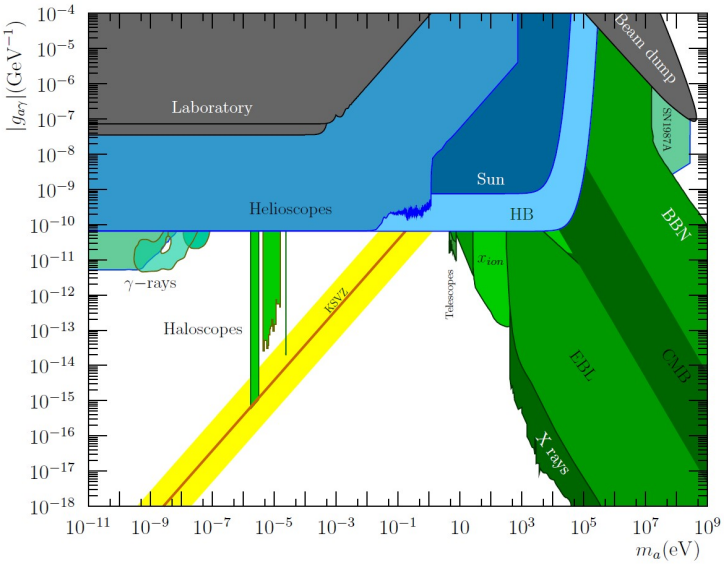

Figure 5: Current constraints on the $g_{a\gamma}$-m_a parameter space. Grey spaces represent laboratory results, blue is used for bounds from helioscope experiments or bounds from stellar physics, green is used for bounds from haloscope experiments or bounds from cosmological considerations and the yellow band gives the QCD-axion band [24].

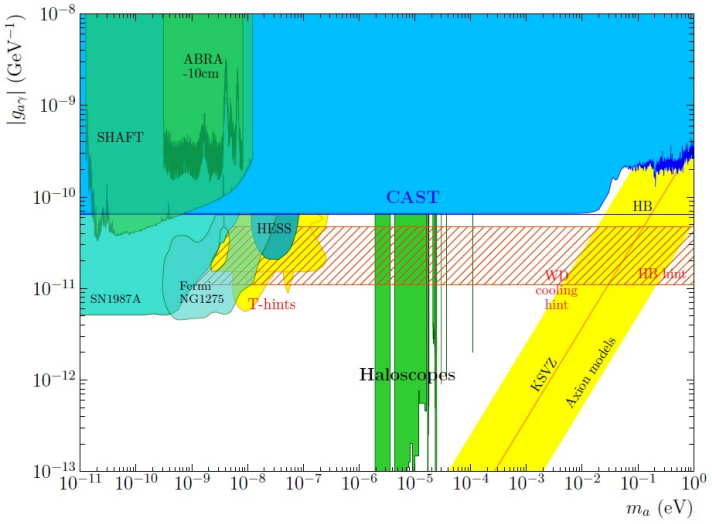

Figure 6: Hinted regions in the $g_{a\gamma}$-m_a parameter space showing the T-hint in yellow and the HB-hint as a red lined band [22].

4 Calculating the axion-photon conversion probability

The calculations of the conversion probability will be explained in the following chapter based on sources [7] and [37]. For all the calculations the natural Lorentz-Heaviside units $c = \hbar = k_B = \epsilon_0 = 1$ will be used as well as $\alpha = \frac{e^2}{4\pi} \approx \frac{1}{137}$ [38].

The calculation of the conversion probability starts with the Lagrangian for the photon-axion interaction. The full interaction Lagrangian can be written as

$$\mathcal{L} = \mathcal{L}_{a\gamma} + \mathcal{L}_a + \mathcal{L}_{EH} \tag{4}$$

where

$$\mathcal{L}_{a\gamma} = \frac{1}{4} a g F_{\mu\nu} \tilde{F}^{\mu\nu} \tag{5}$$

describes the mixing of photons and axions discussed in chapter 2.1. The mass and kinetic term for the axion is

$$\mathcal{L}_a = \frac{1}{2}(\partial^\mu a \partial_\mu a - m^2 a^2) \tag{6}$$

and

$$\mathcal{L}_{EH} = -\frac{1}{4} F_{\mu\nu} F^{\mu\nu} + \frac{\alpha}{90 m_e^4} \left[(F_{\mu\nu} F^{\mu\nu})^2 + \frac{7}{4} \left(F_{\mu\nu} \tilde{F}^{\mu\nu} \right)^2 \right] \tag{7}$$

is the QED Lagrangian for the photon which is also referred to as the Euler-Heisenberg Lagrangian [20]. The second term of equation (7) occurs due to the polarizability of the vacuum and gives one-loop corrections, it is referred to as Euler-Heisenberg-Weisskopf effective Lagrangian. Here $F_{\mu\nu} = \partial_\mu A_\nu - \partial_\nu A_\mu$ denotes the field strength tensor of the magnetic field A_μ and $\tilde{F}_{\mu\nu} = \frac{1}{2}\epsilon_{\mu\nu\rho\lambda} F_{\rho\lambda}$ is its dual [39]. The constants α and m_e refer to the fine-structure constant and electron mass, respectively. The pseudo-scalar axion field is described by a with the photon-axion coupling strength $g_{a\gamma}$ and the axion mass m_a.

From the Lagrangian density (4) the beam propagation equation can be derived. For now a monochromatic and unpolarised beam with a particle energy E is considered. It propagates through a cold medium which is magnetized and ionized. Additionally the external magnetic field is assumed to be homogeneous [7]. Without loss of generality, it can further be assumed that the beam consists of axions propagating along the z-direction.The beam propagation equation is then given by

$$\left(\frac{d^2}{dz^2} + E^2 + 2E\mathcal{M}_0 \right) \Psi(z) = 0 \tag{8}$$

with the wave function

$$\Psi(z) = (A_x(z),\, A_y(z),\, a(z))^T \tag{9}$$

where $A_x(z)$ and $A_y(z)$ describe the amplitudes of the photon field and $a(z)$ the

axion amplitude [7]. $\Psi(z)$ can also be rewritten as

$$\Psi(z) = A_x(z)|\gamma_x\rangle + A_y(z)|\gamma_y\rangle + a(z)|a\rangle \tag{10}$$

with the basis $|\gamma_x\rangle, |\gamma_y\rangle, |a\rangle$ which can be defined as

$$|\gamma_x\rangle = (1,\, 0,\, 0)^T \tag{11}$$
$$|\gamma_y\rangle = (0,\, 1,\, 0)^T \tag{12}$$
$$|a\rangle = (0,\, 0,\, 1)^T. \tag{13}$$

The mixing matrix $\mathcal{M}_0$ is given by

$$\mathcal{M}_0 = \begin{pmatrix} \Delta_{xx} & \Delta_{xy} & \Delta_{a\gamma}^x \\ \Delta_{yx} & \Delta_{yy} & \Delta_{a\gamma}^y \\ \Delta_{a\gamma}^x & \Delta_{a\gamma}^y & \Delta_a \end{pmatrix} \tag{14}$$

with $\Delta_{a\gamma}^x = \frac{gB_x}{2}$ and $\Delta_{a\gamma}^y = \frac{gB_y}{2}$ referring to the mixing of photons and axions where B_x and B_y are the components of the magnetic field [7]. The kinetic axion term is given by $\Delta_a = -\frac{m^2}{2E}$. As the conversion from axion to photon or vice versa is only possible with a magnetic field component transversal to the direction of propagation, the z-component of the magnetic field is not considered here. Additionally, as the magnetic field is assumed to be homogeneous, it can be chosen to be along the y-axis, therefore $B_x = 0$ and $\Delta_{a\gamma}^x = 0$. The remaining magnetic field component B_y will now be referred to only as B, and $\Delta_{a\gamma}^y$ will be referred to as $\Delta_{a\gamma} = \frac{1}{2}gB$. The entries $\Delta_{a\gamma}$ and Δ_a are given by the interaction Lagrangian, while the other entries result from the medium the beam propagates through. The off-diagonal elements Δ_{xy} and Δ_{yx} describe the mixing of the two photon polarisation states in a magnetic field parallel to the direction of propagation which is called Faraday rotation [41]. This effect can be neglected here,therefore $\Delta_{xy} = \Delta_{yx} = 0$ can be omitted. The remaining elements Δ_{xx} and Δ_{yy} contain several different terms which result from different physical effects [37] and will be referred to as $\Delta_\perp$ and $\Delta_\parallel$ respectively. The terms contained in $\Delta_\perp$ and $\Delta_\parallel$ are due to QED vacuum polarisation, plasma effects and interactions of photons in the beam with photons of the CMB [42]. In the literature some of these effects are neglected and there are different formulas given. For $\Delta_\parallel$ there are

$$\Delta_\parallel = 0 \quad [26] \tag{15}$$
$$\Delta_\parallel = \Delta_{\mathrm{pl}} \quad [43] \tag{16}$$
$$\Delta_\parallel = \Delta_{\mathrm{pl}} + \frac{7}{2}\Delta_{\mathrm{QED}} \quad [44] \tag{17}$$
$$\Delta_\parallel = \Delta_{\mathrm{pl}} + \frac{7}{2}\Delta_{\mathrm{QED}} + \Delta_{\mathrm{CMB}} \quad [42]. \tag{18}$$

The term $\Delta_{\mathrm{pl}} = -\frac{\omega_{\mathrm{pl}}^2}{2E}$ is due to the plasma the beam is propagating through where $\omega_{\mathrm{pl}}^2 = \frac{4\pi e^2 n_e}{m_e}$ is the plasma frequency with n_e being the electron density in the plasma and m_e and e being the electron mass and elementary charge respectively [42]. The

additional term $\Delta_{\mathrm{QED}} = \frac{\alpha E}{45\pi}\left(\frac{B}{B_{\mathrm{cr}}}\right)^2$ is the contribution from QED effects, it is related to the effective mass squared of transversal photons $m_\gamma^2 = -\frac{7}{45\pi}\alpha E^2\left(\frac{B}{B_{\mathrm{cr}}}\right)^2$.This mass arises when electrons and photons interact with an external magnetic field of critical field strength $B_{\mathrm{cr}} = \frac{m_e^2}{e} \approx 4.4 \cdot 10^{13}$ G.We can also rewrite $\frac{7}{2}\Delta_{\mathrm{QED}} = -\frac{m_\gamma^2}{2E}$ in a form similar to Δ_{pl} [44]. The last contribution is $\Delta_{\mathrm{CMB}} = \frac{44\alpha^2}{135m_e^4}\rho_{\mathrm{CMB}}E$ with the energy density of the CMB being $\rho_{\mathrm{CMB}} = \frac{\pi^2}{15}T^4 \approx 0.261$ eVcm^{-3} where $T = 2.726$ K is the temperature of the CMB [45]. The term $\Delta_\perp$ won't be relevant for the final conversion probability but for completeness it is given by $\Delta_\perp = \Delta_{\mathrm{pl}} + 2\Delta_{\mathrm{QED}} + \Delta_{\mathrm{CMB}}$ if all contributing terms are considered [42]. This reduces the mixing matrix to

$$\mathcal{M}_0 = \begin{pmatrix} \Delta_\perp & 0 & 0 \\ 0 & \Delta_\parallel & \Delta_{a\gamma} \\ 0 & \Delta_{a\gamma} & \Delta_a \end{pmatrix} \quad [37]. \tag{19}$$

For the calculation of the conversion probability we calculate the eigenvalues and eigenvectors of this mixing matrix [7]. The eigenvalues are

$$\lambda_1 = \Delta_\perp \tag{20}$$

$$\lambda_2 = \frac{1}{2}\left(\Delta_\parallel + \Delta_a - \Delta_{\mathrm{osc}}\right) \tag{21}$$

$$\lambda_3 = \frac{1}{2}\left(\Delta_\parallel + \Delta_a + \Delta_{\mathrm{osc}}\right) \tag{22}$$

where

$$\Delta\mathrm{osc} = \sqrt{(\Delta_\parallel - \Delta_a)^2 + 4\Delta_{a\gamma}^2} \tag{23}$$

is the wave number [37]. The eigenvectors are then given by

$$\vec{x}_1 = (1,\, 0,\, 0)^T \tag{24}$$

$$\vec{x}_2 = (0,\, \Delta_{a\gamma},\, \frac{1}{2}(-\Delta_\parallel + \Delta_a - \Delta_{\mathrm{osc}})^T \tag{25}$$

$$\vec{x}_3 = (0,\, \Delta_{a\gamma},\, \frac{1}{2}(-\Delta_\parallel + \Delta_a + \Delta_{\mathrm{osc}})^T. \tag{26}$$

The wave function is then given by

$$\Psi(z) = c_1\vec{x}_1 e^{\lambda_1(z-z_0)} + c_2\vec{x}_2 e^{\lambda_2(z-z_0)} + c_3\vec{x}_3 e^{\lambda_3(z-z_0)} \tag{27}$$

where z_0 can be referred to as a starting position. By writing $\Psi(z_0)$ in the given form, the exponentials are eliminated and the coefficients c_1, c_2 and c_3 can be calcu-

lated.They are

$$c_1 = A_x(z_0) \tag{28}$$

$$c_2 = \frac{1}{\Delta_{\text{osc}}}\left(\frac{1}{2\Delta_{a\gamma}}(-\Delta_{\parallel} + \Delta_a + \Delta_{\text{osc}})A_y(z_0) - a(z_0)\right) \tag{29}$$

$$c_3 = \frac{1}{\Delta_{\text{osc}}}\left(\frac{1}{2\Delta_{a\gamma}}(-\Delta_{\parallel} + \Delta_a - \Delta_{\text{osc}})A_y(z_0) + a(z_0)\right) \tag{30}$$

Another representation of $\Psi(z)$ will be introduced shortly but first we return to the beam propagation equation (8). As the photons and axions we are interested in have a energy which is much higher than the axion mass, the short-wavelength approximation can be used and the beam propagation equation can be rewritten as

$$\left(\frac{d^2}{dz^2} + E^2\right) = \left(i\frac{d}{dz} + E\right)\left(-i\frac{d}{dz} + E\right) = 2E\left(i\frac{d}{dz} + E\right). \tag{31}$$

This transforms the second-order beam equation into a first-order one

$$\left(i\frac{d}{dz} + E + \mathcal{M}_0\right)\Psi(z) = 0. \tag{32}$$

This is a Schrödinger-like equation and has a lot of similarity with a three-state nonrelativistic quantum system with the three-dimensional wave function $\Psi(z)$ where the z-component replaces the time-component [7]. With the Hamiltonian $H = -(E + \mathcal{M}_0)$ this leads to $i\frac{d}{dz}\Psi(z) = H\Psi(z)$ which is solved by

$$\Psi(z) = U_0(z, z_0)\Psi(0) \tag{33}$$

where $U_0(z, z_0)$ is called transfer matrix. The transfer matrix can be rewritten as

$$U_0(z, z_0) = e^{iE(z-z_0)}\mathcal{U}_0(z, z_0) \tag{34}$$

where $\mathcal{U}_0(z, z_0)$ is the transfer matrix belonging to the reduced Schrödinger-like equation

$$(id_z + \mathcal{M}_0)\,\Psi(z) = 0. \tag{35}$$

This transfer matrix can be rewritten as

$$\mathcal{U}_0(z, z_0) = T_1(0)e^{i\lambda_1(z-z_0)} + T_2(0)e^{i\lambda_2(z-z_0)} + T_3(0)e^{i\lambda_3(z-z_0)} \tag{36}$$

and therefore

$$\Psi(z) = T_1(0)e^{i\lambda_1(z-z_0)}\Psi(z_0) + T_2(0)e^{i\lambda_2(z-z_0)}\Psi(z_0) + T_3(0)e^{i\lambda_3(z-z_0)}\Psi(z_0). \tag{37}$$

With the representation (27) of the wave function and the constants (28-30) the matrices $T_1 - T_3$ can be calculated to be

$$\mathcal{T}_1 = \begin{pmatrix} 1 & 0 & 0 \\ 0 & 0 & 0 \\ 0 & 0 & 0 \end{pmatrix}, \tag{38}$$

$$\mathcal{T}_2 = \begin{pmatrix} 0 & 0 & 0 \\ 0 & \lambda_3 - \Delta_\parallel & -\Delta_{a\gamma} \\ 0 & \frac{1}{\Delta_{a\gamma}}(\lambda_2 - \Delta_\parallel)(\lambda_3 - \Delta_\parallel) & -(\lambda_2 - \Delta_{a\gamma}) \end{pmatrix}, \tag{39}$$

$$\mathcal{T}_3 = \begin{pmatrix} 0 & 0 & 0 \\ 0 & -(\lambda_2 - \Delta_\parallel) & \Delta_{a\gamma} \\ 0 & -\frac{1}{\Delta_{a\gamma}}(\lambda_2 - \Delta_\parallel)(\lambda_3 - \Delta_\parallel) & \lambda_3 - \Delta_{a\gamma} \end{pmatrix}. \tag{40}$$

To rewrite these in a simpler form the photon-axion mixing angle α is introduced. It is given by

$$\alpha = \frac{1}{2} \arctan\left(\frac{2\Delta_{a\gamma}}{\Delta_\parallel - \Delta_a}\right) \quad [7] \tag{41}$$

The three matrices $T_1 - T_3$ written in terms of this angle are

$$\mathcal{T}_1 = \begin{pmatrix} 1 & 0 & 0 \\ 0 & 0 & 0 \\ 0 & 0 & 0 \end{pmatrix}, \tag{42}$$

$$\mathcal{T}_2 = \begin{pmatrix} 0 & 0 & 0 \\ 0 & \sin^2(\alpha) & -\sin(\alpha)\cos(\alpha) \\ 0 & -\sin(\alpha)\cos(\alpha) & \cos^2(\alpha) \end{pmatrix}, \tag{43}$$

$$\mathcal{T}_3 = \begin{pmatrix} 0 & 0 & 0 \\ 0 & \cos^2(\alpha) & \sin(\alpha)\cos(\alpha) \\ 0 & \sin(\alpha)\cos(\alpha) & \sin^2(\alpha) \end{pmatrix} \tag{44}$$

which can be used to express the transfer matrix $\mathcal{U}_0(y, y_0)$ in the way presented in equation (36) [7].

The conversion probability for a photon polarized along the y-axis oscillating into an axion after propagating the distance z through a constant, homogeneous magnetic field is given by

$$P_{0,\gamma\to a}(z) = \left|\langle a \left|\mathcal{U}_0(z,0)\right| \gamma_y\rangle\right|^2. \tag{45}$$

With the states $\gamma_y\rangle$ and $|a\rangle$ are given in (12) and (13), respectively, the probability is

$$P_{0,\gamma\to a}(z) = \left|\sin(\alpha)\cos(\alpha)\left(e^{i\lambda_3 z} - e^{i\lambda_2 z}\right)\right|^2. \tag{46}$$

Using the double-angle formula $\sin(2\alpha) = 2\sin(\alpha)\cos(\alpha)$ as well as rewriting the

exponentials in form of a sine results in

$$P_{0,\gamma\to a}(z) = \frac{4\Delta_{a\gamma}^2}{\Delta_{\text{osc}}^2}\sin^2\left(\frac{1}{2}z\Delta_{\text{osc}}\right). \tag{47}$$

Depending on the different expressions for $\Delta_{||}$ which is contained in Δ_{osc} the exact expression for the conversion probability varies.

Until now the photon beam was assumed to be polarised and the magnetic field to be constant along the propagated distance. In reality the problem is slightly more difficult to solve. There is no reason for the beam to be polarised as it was assumed above, therefore an unpolarised beam has to be considered [7]. It is described by a generalised polarisation density $\rho(z) = \Psi(z)\Psi(z)^\dagger$ which obeys the Von Neumann-like equation $id_z\rho(z) = [\rho, \mathcal{M}_0]$ which is solved by

$$\rho(z) = \mathcal{U}_0(z, z_0)\rho(z_0)\mathcal{U}_0(z, z_0)^\dagger. \tag{48}$$

The probability for a photon or axion converting from state ρ_1 to ρ_2 after a distance z is given by

$$P_{0,\rho_1\to\rho_2}(z) = \text{Tr}\left(\rho_2\mathcal{U}_0(z,0)\rho_1\mathcal{U}_0(z,0)^\dagger\right) \tag{49}$$

where we assume ρ_1 and ρ_2 to each have a trace of 1 [7].

Additionally the magnetic field might not be aligned with the y-axis [7]. Therefore the total path length z will be divided into domains of equal length s in which the strength of the magnetic field is constant but its orientation is assumed to be random in each of the domains. The basis for this calculation can be found in [46]. The wave function in the initial state $\Psi(0)$ is written in same form as in equation (10) and can be used to calculate the initial photon and axion fluxes which are given by

$$I_\gamma(0) \sim |A_x(0)|^2 + |A_y(0)|^2 \tag{50}$$

$$I_a(0) \sim |a(0)|^2. \tag{51}$$

In the initial domain the magnetic field is assumed to be aligned with $|\gamma_y\rangle$, this is not the case in a random domain n. As the only relevant component of the magnetic field is the one perpendicular to $|a\rangle$, the direction of the perpendicular magnetic field $B_\perp$ is rotated by an arbitrary angle ϕ_n in the plane perpendicular to $|a\rangle$. The axes are now rotated such that the axis $|\gamma_{||}^{(n)}\rangle$ and $|\gamma_\perp^{(n)}\rangle$ are parallel and perpendicular to $B_\perp$ respectively. They can be expressed through the initial axis $|\gamma_x\rangle$ and $|\gamma_y\rangle$ by

$$|\gamma_{||}^{(n)}\rangle = \cos(\phi_n)|\gamma_x\rangle + \sin(\phi_n)|\gamma_y\rangle \tag{52}$$

$$|\gamma_\perp^{(n)}\rangle = -\sin(\phi_n)|\gamma_x\rangle + \cos(\phi_n)|\gamma_y\rangle. \tag{53}$$

The state in the n-th domain is then given by

$$\Psi(z_n) = A_x(z_n)\left(c_n|\gamma_x\rangle + s_n|\gamma_y\rangle\right) + A_y(z_n)\left(-s_n|\gamma_x\rangle + c_n|\gamma_y\rangle\right) + a(z_n)|a\rangle \tag{54}$$

where c_n and s_n refer to $\cos(\phi_\gamma)$ and $\sin(\phi_\gamma)$ respectively. The distance $z_n = (n-1)s$

is the distance from the origin of the beam to the beginning of the n-th domain [46]. The fluxes at the beginning of the n-th domain can be written as

$$I_\gamma(n) = |A_x(z_n)|^2 + |A_y(z_n)|^2 \tag{55}$$
$$I_a(n) = |a(z_n)|^2. \tag{56}$$

As photons convert into axions and axions into photons with the conversion probability P_0 given in equation (47), the fluxes at the end of the n-th domain or at the beginning of the $(n+1)$-th domain are

$$I_\gamma(n+1) = (1 - P_0 c_n^2)|A_x(z_n)|^2 + (1 - P_0 s_n^2)|A_y(z_n)|^2 + P_0|a(z_n)|^2 ... \tag{57}$$
$$I_a(n+1) = P_0 c_n^2 |A_x(z_n)|^2 + P_0 s_n^2 |A_y(z_n)|^2 + (1 - P_0)|a(z_n)|^2 .... \tag{58}$$

The ellipsis refers to terms proportional to c_n, s_n or $c_n s_n$ which we now averaged to zero. This is allowed because of randomness of magnetic field [46]. In the same way c_n^2 and s_n^2 can be averaged to $1/2$ which leads to

$$I_\gamma(n+1) = (1 - 1/2P_0)\left(|A_x(z_n)|^2 + |A_y(z_n)|^2\right) + P_0|a(z_n)|^2 \tag{59}$$
$$I_a(n+1) = 1/2P_0\left(|A_x(z_n)|^2 + |A_y(z_n)|^2\right) + (1 - P_0)|a(z_n)|^2. \tag{60}$$

Utilizing equation (56) the fluxes at the end of the n-th domain can be expressed as

$$\begin{pmatrix} I_\gamma(n+1) \\ I_a(n+1) \end{pmatrix} = \begin{pmatrix} 1 - 1/2P_0 & P_0 \\ 1/2P_0 & 1 - P_0 \end{pmatrix} \begin{pmatrix} I_\gamma(n) \\ I_a(n) \end{pmatrix} \tag{61}$$
$$= \begin{pmatrix} 1 - 1/2P_0 & P_0 \\ 1/2P_0 & 1 - P_0 \end{pmatrix}^{(n+1)} \begin{pmatrix} I_\gamma(0) \\ I_a(0) \end{pmatrix}. \tag{62}$$

To calculate the exponential of the matrix, it can be rewritten as

$$\begin{pmatrix} 1 - 1/2P_0 & P_0 \\ 1/2P_0 & 1 - P_0 \end{pmatrix}^{(n+1)} = \left(\mathbb{1} - \frac{P_0}{2}\begin{pmatrix} 1 & -2 \\ -1 & 2 \end{pmatrix}\right)^{(n+1)} \tag{63}$$
$$= \left(\mathbb{1} - \frac{P_0}{2}A\right)^{(n+1)} \tag{64}$$

and as $\mathbb{1}$ and the matrix A commute, the binomial theorem can be used for this calculation. For $k \geq 1$ the matrix exponential A^k is given by $A^k = 3^{(k-1)}A = \frac{3^k}{3}A$. In total this leads to

$$\begin{pmatrix} I_\gamma(n+1) \\ I_a(n+1) \end{pmatrix} = \frac{1}{3}\begin{pmatrix} 2 + (1 - 3/2P_0)^{(n+1)} & 2 - 2(1 - 3/2P_0)^{(n+1)} \\ 1 - (1 - 3/2P_0)^{(n+1)} & 1 + 2(1 - 3/2P_0)^{(n+1)} \end{pmatrix} \quad [46]. \tag{65}$$

Additionally as $P_0 \ll 1$ and the number of domains is large $(1 - 3/2P_0)^{(n+1)}$ can be rewritten as $\exp\left(-\frac{3}{2}P_0(n+1)\right)$ or rather $\exp\left(-\frac{3}{2}P_0\frac{z}{s}\right)$ where the ratio z/s gives the

number of domains crossed by the beam. Finally the fluxes can be rewritten to

$$I_\gamma(z) = I_\gamma(0) - \frac{1}{3}\left(1 - e^{(-\frac{3}{2}P_0\frac{z}{s})}\right)(I_\gamma(0) - 2I_a(0)) \tag{66}$$

$$= I_\gamma(0) - P_{\gamma\to a}(I_\gamma(0) - 2I_a(0)) \tag{67}$$

$$I_a(z) = I_a(0) + \frac{1}{3}\left(1 - e^{(-\frac{3}{2}P_0\frac{z}{s})}\right)(I_\gamma(0) - 2I_a(0)) \tag{68}$$

$$= I_a(0) + P_{\gamma\to a}(I_\gamma(0) - 2I_a(0)) \tag{69}$$

where

$$P_{\gamma\to a} = \frac{1}{3}\left(1 - e^{-\frac{3}{2}P_0\frac{z}{s}}\right) \tag{70}$$

is the probability for axion-photon conversion after propagation through $N = \frac{z}{s}$ domains of randomly oriented magnetic fields of equal strength referred to as magnetic field domains [46].

5 Analysis of the conversion probability

5.1 Parameters and current bounds

The conversion probability in equation (70) depends on a total of seven parameters. There are six physical parameters,

- axion mass m_a
- coupling strength $g_{a\gamma}$
- axion energy E
- coupling strength B
- electron density n_e
- distance of propagation z.

From now on the distance of propagation will be referred to as the luminosity distance D_L. Additionally there is the unphysical parameter s referring to the length of magnetic field domains. In each of the domains the angle between the magnetic field and the axis of the x-polarisation of the photon-beam is chosen randomly between 0 and 2π. To reduce the number of parameters to six while still providing a significant sample size of random magnetic field orientations the number of domains is set to $N = \frac{D_L}{s} = 100$. As the luminosity distance D_L is randomly generated, the domain length s is varied as well. The remaining parameters need to be limited to relevant ranges.

The magnetic field and electron density vary depending on the medium which the particles propagate through from their source towards earth. If a source is located in the Milky Way, particles only propagate through galactic medium where both magnetic field strength and electron density are comparably high. Particles can also originate from further distant sources located beyond the Milky Way. Such sources might be located in the Local Group, the galaxy cluster containing the Milky Way, or the Virgo Supercluster, which is the supercluster containing the Local Group and the Virgo Cluster. Particles from sources in these regions propagate mainly through intracluster medium where both the magnetic field strength and the electron density are slightly lower compared to the ones in the galactic medium. Particles from sources even beyond these structures propagate mostly through empty space where magnetic field strength and electron density are comparably low. Therefore it is reasonable to perform calculations for three different categories of particle origin: the void, cluster and Galaxy scenario. But even in galaxies there are differences especially in the electron density. In the galactic disk the electron density can be considerably higher than on the edges of a galaxy, therefore the Galaxy scenario is split into two scenarios, one with high and one with low electron density resulting in a total of four categories.

Typical galaxies have diameters up to 10^2 kpc. The Milky Way is comparably small and has a diameter of $\approx$ 30kpc but for the following calculations the distance range is set to $10^0 - 10^3$ kpc to include sources located not in but close to the Milky Way as well.

The electron density can reach up to $n_e = 0.015$ cm^{-3} in the galactic disk [48] but might be as low as $n_e = 10^{-11} - 10^{-8}$ cm^{-3} at the edges of the galaxy [49]. For the

high and low electron density scenarios the parameter ranges $n_e = 10^{-3} - 10^{-1}$ cm^{-3} and $n_e = 10^{-11} - 10^{-8}$ cm^{-3} will be used, respectively. Typical magnetic fields in other spiral galaxies are $B = 13.5 \pm 5.5$ μG but might be around $B \approx 6$ μG for galaxies with moderate star formation or up to $B = 50-300$ μG for starburst galaxies [41]. The Milky Way is a spiral galaxy but with a generous estimate the range of the magnetic field will be set to $B = 10^0 - 10^3$ μG for both of the Galaxy scenarios.

For source candidates beyond the Milky Way but in the Local Group or the Virgo Supercluster the distance range is set to $10^3 - 10^4$ kpc. Particles from sources in these regions propagate mainly through intracluster medium (ICM) where the magnetic field is of similar or weaker strength than in the galaxies themselves at around $B = 0.2 - 10\mu$G [50]. For the cluster scenario the parameter range will be set to $B = 10^{-1} - 10^2\mu$G. As in the low electron density Galaxy scenario the electron density will be set to $n_e = 10^{-11} - 10^{-8}$ cm^{-3}.

Sources located beyond a galactic void have distances above 10^4 kpc. The distance range for the calculations will be set to $10^4 - 10^7$ kpc, sources beyond 10^7 kpc will not be considered here. Particles from sources in the void scenario propagate mostly through empty space where the strength of magnetic fields is $B \approx 10^{-9}\mu$G [51], therefore the parameter range will be set to $B = 10^{-9} - 10^{-6}\mu$G. The electron density again is assumed to be in the range $n_e = 10^{-11} - 10^{-8}$ cm^{-3} [49].

For the axion mass and coupling strength the parameter ranges are set to $m = 10^{-12} - 10^{12}$ neV and $g_{a\gamma} = (10^{-19} - 10^1) \cdot 10^{-11}$ GeV^{-1} for all of the scenarios mentioned above [52],[17],[26]. These are based on the current bounds on the axion mass-coupling strength parameter space displayed in Fig. 5. The parameter space is chosen in a way to cover the mostly white area in the plot which has not been investigated by experiments yet. The upper limits of the axion mass and coupling strength are marked as red lines in Fig. 7.

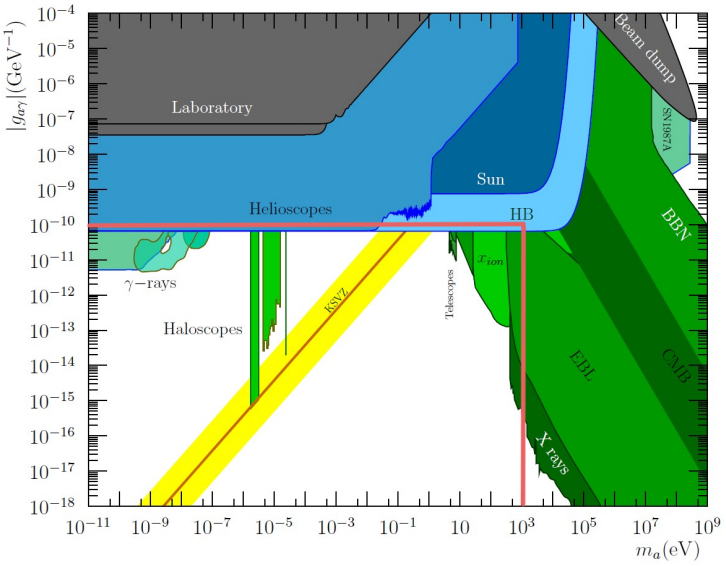

Figure 7: Current constraints on the axion mass-coupling strength parameter space with marked parameter ranges for axion mass and coupling strength chosen for the following calculation [24].

The particles energy range is set to $E = 10^5 - 10^{13}$ GeV for all of the scenarios to cover a broad energy spectrum. For a better overview the parameter ranges for each of the scenarios are displayed in Tab. 1.

parameter ranges	void	cluster	galaxy (low electron density)	galaxy (high electron density)
distance [kpc]	$10^4 - 10^7$	$10^3 - 10^4$	$10^0 - 10^3$	
electron density [cm^{-3}]	$10^{-11} - 10^{-8}$	$10^{-11} - 10^{-8}$	$10^{-11} - 10^{-8}$	$10^{-3} - 10^{-1}$
magnetic field strength [μG]	$10^{-9} - 10^{-6}$	$10^{-1} - 10^2$	$10^0 - 10^3$	
coupling strength [10^{-11} GeV^{-1}]	$10^{-19} - 10^1$			
axion mass [neV]	$10^{-12} - 10^{12}$			
energy [GeV]	$10^5 - 10^{13}$			

Table 1: Parameter ranges chosen for the four different scenarios.

5.2 Calculating and modelling the photon-axion conversion

The parameters are now set to specific ranges but scanning the conversion probability along all of these parameters is computationally intensive. Varying each parameter independently in reasonably small steps leads to an unreasonably large number of calculations. By choosing larger steps for the variation of the parameters, small-scale features of the conversion probability could be missed. Instead of only varying one parameter at a time, all of the parameters are varied simultaneously by choosing each of them randomly in their respective interval. The conversion probability is then calculated utilizing the gammaALPs python package [35]. For each of the four scenarios mentioned in the previous chapter, 101101 random parameter sets are generated and their corresponding conversion probabilities are calculated. The results of the calculation can be displayed in individual 1D histograms for each of the scenarios which are displayed in Fig. 8. In the plots the mean value, the root mean square (RMS) and the median are marked.

As one might expect, all four diagrams look similar. In the plots for the two Galaxy scenarios, there are no differences noticeable. The mean value, RMS and median are at the same positions. Between the Galaxy scenarios and the cluster scenario there are only slight differences. All three of the marked lines are shifted to slightly higher values for the cluster scenario. For the void scenario the differences are more noticeable. The overall shape of the envelop function is still similar but the marked lines are all several orders of magnitude lower compared to the other scenarios. This indicates that it is rather unlikely that axion-photon conversion takes place in galactic voids. For particles propagating through galaxy or cluster medium, a conversion is much more likely. The differences between the scenarios are due to the different parameter ranges for distance and magnetic field strength.

To study the effects of each of the parameters on the conversion probability, 2D histograms are helpful. They display one parameter against the conversion probabil-

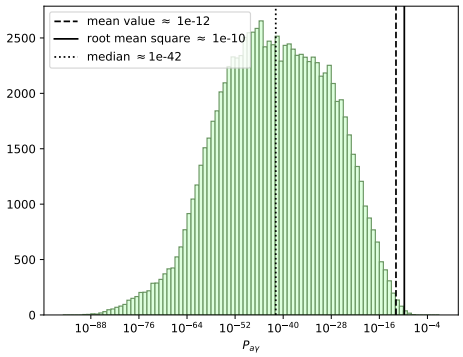

(a) Void scenario: distance $D_L = 10^4 - 10^7$ kpc, magnetic field $B = 10^{-9} - 10^{-6}$ μG, electron density $n_e = 10^{-11} - 10^{-8}\text{cm}^{-3}$

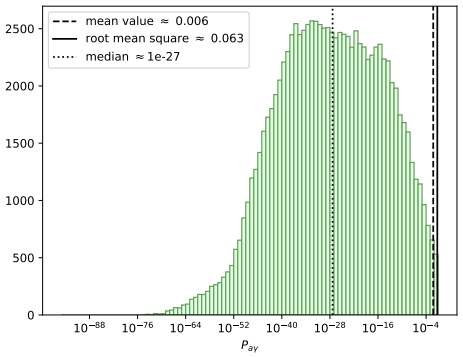

(b) Cluster scenario: distance $D_L = 10^3 - 10^4$ kpc, magnetic field $B = 10^{-1} - 10^2$ μG, electron density $n_e = 10^{-11} - 10^{-8}\text{cm}^{-3}$

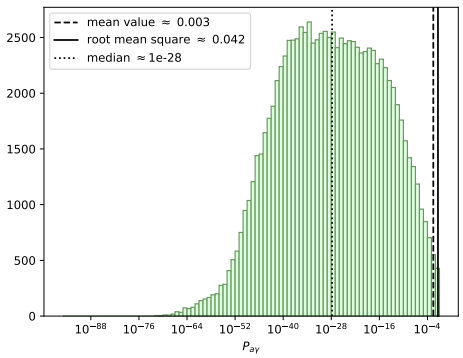

(c) Galaxy scenario: distance $D_L = 10^0 - 10^3$ kpc, magnetic field $B = 10^0 - 10^3$ μG, electron density $n_e = 10^{-11} - 10^{-8}\text{cm}^{-3}$

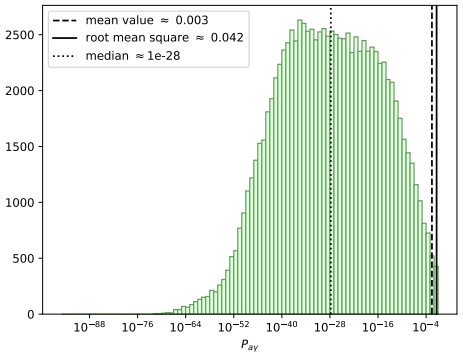

(d) Galaxy scenario with high electron density: distance $D_L = 10^0 - 10^3$ kpc, magnetic field $B = 10^0 - 10^3$ μG, electron density $n_e = 10^{-3} - 10^{-1}\text{cm}^{-3}$

Figure 8: Histograms of the conversion probability for the different categories (from top left to bottom right) void, cluster, Galaxy with low electron density and Galaxy with high electron density.

ity to evaluate the effect that each single parameter has on the result. The number of data points is displayed on the colour-axis. The 2D histograms for the cluster scenario are displayed in Fig. 9, the plots for the other scenarios can be found in Appendix A. Additionally profile plots are added to analyse the effect of the parameter on the conversion probability in more detail.

Here the differences and similarities between the scenarios are noticeable as well. The conversion probabilities for the void scenario accumulate at lower values than for the other scenarios. It is again noticeable that there is no visible difference between the plots for the two Galaxy scenarios which are only distinguished by the electron density. The effect of the electron density on the resulting conversion probability seems negligible and the Galaxy scenario with high electron density will be omitted in further discussion. Not only does the electron density variation show no effect between the two Galaxy scenarios but for the other scenarios the histograms for the electron density show only a statistical distribution which is due to the variation of the other parameters. The situation for the magnetic field and distance looks similar, there seems to be mostly a statistical distribution. The profile plots for the distance show an almost flat curve but it is important to notice here that the distance is varied only over $1-3$ magnitudes in each of the scenarios which could be the reason for the barely noticeable effects. Additionally the distance only contributes in the sine term of the conversion probability in equation (70) due to setting $N = \frac{z}{s} = 100$.

In the profile plot for the magnetic field strength shown in Fig. 9a and in the respective subfigures of Figs. 24-25 it is interesting to notice that the conversion probability rises with the magnetic field strength in the void scenario while in the cluster scenario the conversion probability increases up to $B \approx 10^{0.5}$ μG and then decreases again for higher magnetic field strengths which is visible in the histogram for the cluster scenario and the Galaxy scenario. This effect is mostly likely due to the contribution of the magnetic field strength in both the numerator and denominator of the fraction $\frac{3\Delta_{a\gamma}^2}{\Delta_{\mathrm{osc}}^2}$ in equation (47). In the term Δ_{osc} the magnetic field strength is summand, it might be overpowered by some of the other summands for low values. Therefore the numerator might provide the leading effect resulting in the increase of the conversion probability for low values of the magnetic field strength. Above $B \approx 10^{0.5}$ μG, the contribution of the magnetic field strength in the denominator might increase to overpower the other summands making it the leading effect which shows in the slight decrease of the coupling strength below this threshold.

The effects of the remaining parameters, the particle energy, axion mass and coupling strength are the most noticeable. The logarithm of the conversion probability grows linear with the logarithm of the coupling strength and decreases linearly with the logarithm of the energy. This means the conversion probability increases and decreases exponentially with coupling strength and energy, respectively. For low axion masses the conversion probability seems to be unaffected by the variation of the axion mass, the distribution seems statistical. For higher axions masses above a certain threshold the conversion probability decreases exponentially. This behaviour is due to the axion mass being part of a summand in the denominator of $\frac{3\Delta_{a\gamma}^2}{\Delta_{\mathrm{osc}}^2}$ in equation (47). For low values it is overpowered by other summands and only has a contributing effect above a certain threshold. This threshold axion mass varies between the scenarios. For the void scenario it is $m_{threshold} \approx 10^{4.5}$ neV, for the other scenarios it is slightly lower at $m_{threshold} \approx 10^{4}$ neV for the Galaxy scenarios and

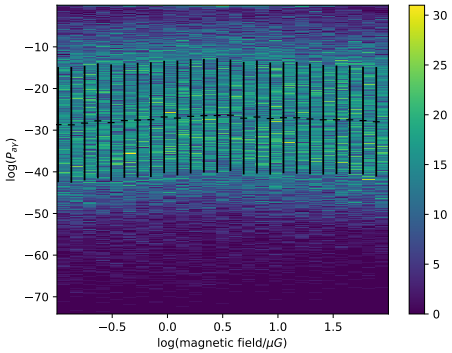

(a) 2D histogram displaying conversion probability against magnetic field strength.

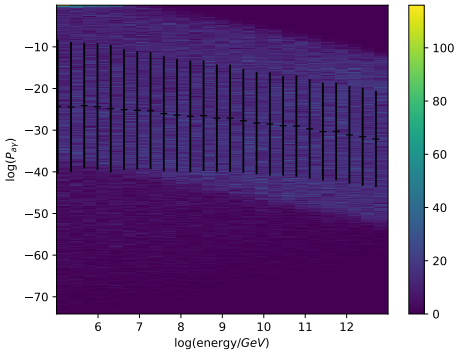

(b) 2D histogram displaying conversion probability against particle energy.

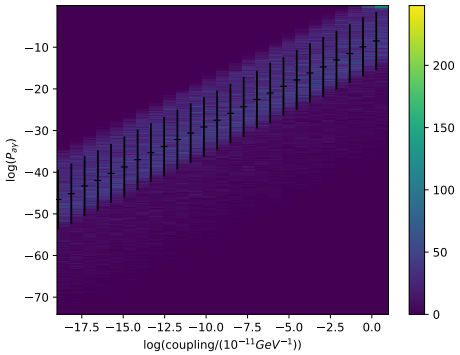

(c) 2D histogram displaying conversion probability against coupling strength.

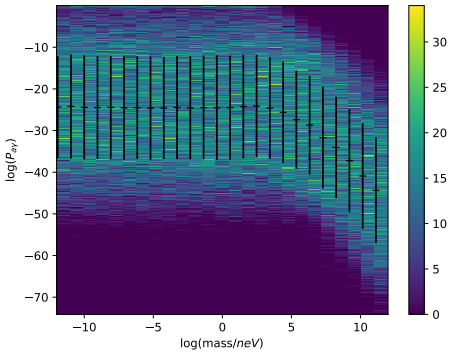

(d) 2D histogram displaying conversion probability against axion mass.

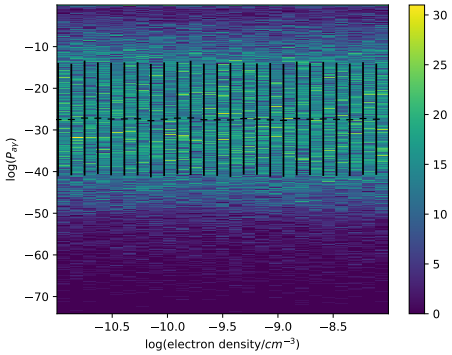

(e) 2D histogram displaying conversion probability against electron density.

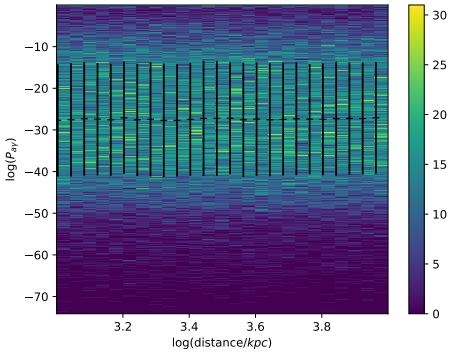

(f) 2D histogram displaying conversion probability against luminosity distance.

Figure 9: 2D histograms for a source located in a galaxy cluster plotting the conversion probability against (from top left to bottom right) magnetic field strength, axion energy, coupling strength, axion mass, electron density, distance.

$m_{threshold} \approx 10^{3.5}$ neV for the cluster scenario.

5.3 Discussion of possible axion sources

For further discussion some specific axion source candidates are introduced. As mentioned above, possible axions sources are supernovae, AGNs or merger events. One possible event is the neutron star merger observed on August 17th 2017 as the gravitational wave signal GW170817 and as the gamma ray burst GRB 170817. The detection of this event can be considered an enormous breakthrough in the field of multimessenger astronomy as it was the first gravitational wave signal confirmed by the detection of electromagnetic signals. With a distance of $D_L \approx 40$ Mpc this event is located in Hydra-Centaurus supercluster which is the closest neighbouring Supercluster of the Virgo Supercluster. Due to its proximity this event will be discussed in the cluster scenario [53]. Additionally the supernova SN 1885A will be discussed in the same scenario. This event was the first supernova detected from beyond the Milky Way. It is located in the Andromeda galaxy and has a distance of $D_L = 795$ kpc [54].

For a gamma-ray originating from a relatively close source in the Milky Way itself, GRB 980425 can be considered which originated from a source at a distance of $D_L = 13$ kpc [60]. Additionally a supernova event will be discussed here as well. The supernova SN 1987A detected in 1987 occurred at a distance of $D_L = 50$ kpc in the Large Magellanic Cloud, a satellite galaxy of the Milky Way [62]. It is not located in the Milky Way itself but because of its proximity it is placed in the Galaxy scenario. Supernovae emit $\approx 99\%$ of their gravitational binding energy in the form of neutrinos which led to the first observations of neutrinos from a supernova in 1987 when SN 1987A was discovered. Since then the branch of neutrino astronomy grew rapidly contributing to multimessenger astronomy.

For the void scenario, events further outside of the Virgo Supercluster are considered. One possible candidate is the blazar TXS 0506+056 which was first observed in 1983. It originated at a distance of $D_L \approx 1.8$ Gpc and was likely a source of high energy neutrinos [57].

A gamma-ray burst originating from a great distance is GRB 970228 discovered in 1997 which originated at a distance of $D_L = 4.5$ Gpc[58]. Additionally the gravitational wave event GW150914 resulting from the merging of two black holes at a distance of $D_L = 0.4$ Gpc [56] will be discussed. The detection of this event is known as the first direct measurement of a gravitational wave signal and was the first observed binary black hole merger. Together these three distant source candidates will be grouped in the void scenario.

For further calculations not only the conversion probability is relevant but the number of photons converted from axions reaching detectors at earth, especially the Pierre Auger Observatory, is important as well. To calculate this number, the amount of axions emitted at the source is required. Assuming all axions are emitted with a fixed energy E, the number of axions emitted at the source is given by $N_a = \frac{E_{\mathrm{tot,a}}}{E}$ where $E_{\mathrm{tot,a}}$ is the total energy emitted in the form of axions at the source, which will be referred to as axion emission energy. The axion emission energy of the sources is unknown but the total emitted energy E_{tot} is known for many sources, so to have a reference value it will be assumed that the total energy emitted at the source E_{tot}

stems solely from axions resulting in $N_a = \frac{E_{\text{tot}}}{E}$. At a luminosity distance D_L a number $N_{\gamma,tot} = N_a \cdot P = \frac{E_{\text{tot}} \cdot P}{E}$ axions have converted into photons. Here P refers to the calculated conversion probability given in equation (70) which depends on the luminosity distance among other parameters. It can be assumed that the number of photons converted from axions is distributed homogeneously over a sphere of radius D_L. For this study only the number of photons crossing an orthogonal area that roughly corresponds to the aperture of the Pierre Auger Observatory is relevant. The expected number of photons crossing this area is then given by

$$N_\gamma \approx \frac{E_{\text{tot,a}} \cdot P}{E} \cdot \frac{3000 \text{ km}^2}{4\pi D_L^2}. \tag{71}$$

As the total emitted energy and distance are known for the discussed source candidates, the ratio $\frac{E}{P} = \frac{E_{\text{tot,a}}}{N_\gamma} \cdot \frac{3000 \text{ km}^2}{4\pi D_L^2}$ can be calculated for each of them for a given number of photons crossing the detector which is set to $N_\gamma = 1$ for now. The ratio

$$\frac{E}{P} = E_{\text{tot,a}} \frac{3000 \text{ km}^2}{4\pi D_L^2} \tag{72}$$

for the given source candidates can be found in tables 2-4. For the source candidate TXS 0506 +056 there is no information on the total emitted energy but from the neutrino luminosity of $1.2 \cdot 10^{47}$ erg s^{-1} and the six month duration of a flare [57] a total emitted energy during the flare of $\approx 10^{57}$ GeV can be estimated.

Events	luminosity distance D_L [kpc]	total emitted energy E_{tot} [GeV]	total emitted energy E_{tot} [erg], form of energy emission	ratio $\frac{E}{P}$ [GeV]
GW150914	$10^{5.64}$ [56]	$3.5 \cdot 10^{57}$ [56]	$5.61 \cdot 10^{5.4}$ (GW)	$4.5 \cdot 10^{15}$
TXS 0506+056	$10^{6.25}$ [57]	10^{57} from [57]	$1.87 \cdot 10^{57}$ (ν)	$7.9 \cdot 10^{13}$
GRB 970228	$10^{6.66}$ [58]	$3.2 \cdot 10^{54}$[59]	$5.2 \cdot 10^{51}$ (γ)	$3.9 \cdot 10^{10}$

Table 2: Source candidates, distances, total emitted energies and calculated E/P ratio of axion source candidates in the void scenario.

Events	luminosity distance D_L [kpc]	total emitted energy E_{tot} [GeV]	total emitted energy E_{tot} [erg], form of energy emission	ratio $\frac{E}{P}$ [GeV]
GRB 170817	39472 [53]	$2.6 \cdot 10^{49}$ [53]	$4.17 \cdot 10^{46}$ (γ)	$4.2 \cdot 10^{9}$
GW170817	39472 [53]	$4.5 \cdot 10^{55}$ [56]	$7.21 \cdot 10^{52}$ (GW)	$7.2 \cdot 10^{15}$
SN 1885A	795 [54]	$\approx 2 \cdot 10^{56}$ [55]	$3.2 \cdot 10^{53}$ (Ni)	$8.0 \cdot 10^{19}$

Table 3: Source candidates, distances, total emitted energies and calculated E/P ratio of axion source candidates in the cluster scenario.

Now a minimal energy of $E = 10^5$ GeV will be assumed. For this minimal energy a conversion probability, for which the ratio is fulfilled, can be calculated for each of the source candidates. These conversion probabilities necessary for $N = 1$ photon to

Events	luminosity distance D_L [kpc]	total emitted energy E_{tot} [GeV]	total emitted energy E_{tot} [erg], form of energy emission	ratio $\frac{E}{P}$ [GeV]
GRB 980425	13 [60]	$6.2 \cdot 10^{53}$ [61]	$9.93 \cdot 10^{50}$ (γ)	$9.2 \cdot 10^{20}$
SN 1987A	50 [62]	$1.5 \cdot 10^{56}$ [63], [62]	$2.40 \cdot 10^{53}$ (ν)	$3.6 \cdot 10^{22}$

Table 4: Source candidates, distances, total emitted energies and calculated E/P ratio of axion source candidates in the Galaxy scenario.

transverse the detector plane of the Pierre Auger Observatory can be marked in the 1D histograms which can be seen in Fig. 10.

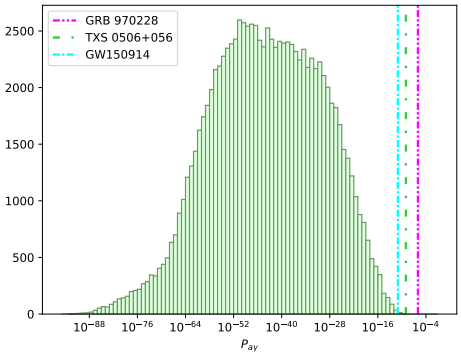

(a) Void scenario.

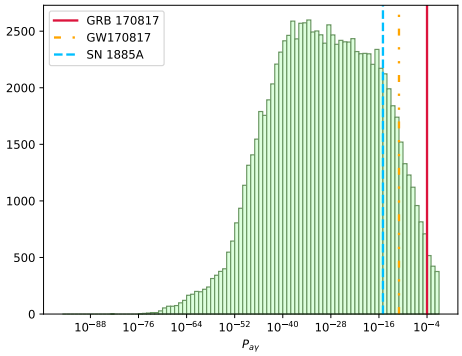

(b) Cluster scenario.

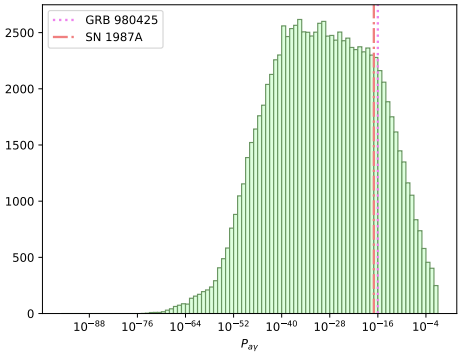

(c) Galaxy scenario.

Figure 10: 1D histogram for the different scenarios with marked conversion probabilities necessary for $N = 1$ photon to traverse the detector plane of the Pierre Auger Observatory at $E = 10^5$ GeV.

For the source candidate GRB 970228 in the void scenario, the highest calculated conversion probability is clearly below the marked threshold. For the source candidates TXS 0506+056 and GW150914 there are only few parameter combinations above the marked thresholds for the respective sources. All of the other source candidates have marked conversion probabilities clearly below the maximum calculated

conversion probabilities.

The lowest photon energy measurable at the Pierre Auger Observatory is $E \approx 10^8$ GeV, it is therefore useful to calculate the conversion probabilities resulting in $N = 1$ photon at the detector for this energy as well [11]. As before the results are displayed in the 1D histogram which can be seen in Fig. 11.

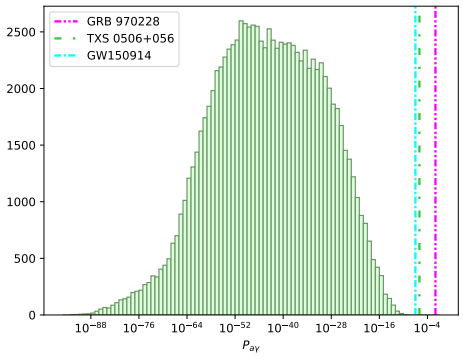

(a) Void scenario.

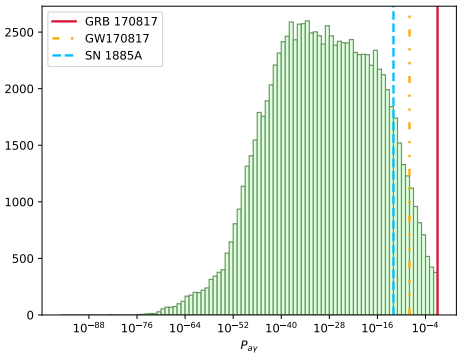

(b) Cluster scenario.

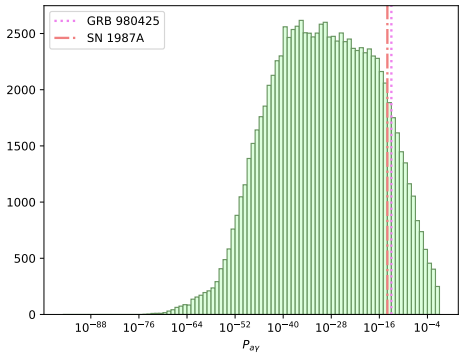

(c) Galaxy scenario.

Figure 11: 1D histogram for the different scenarios with marked conversion probabilities necessary for $N = 1$ photon to traverse the detector plane of the Pierre Auger Observatory at $E = 10^8$ GeV.

For all three source candidates in the void scenario the highest calculated conversion probabilities are clearly below the threshold. Most of the source candidates in the other scenarios have conversion probabilities resulting in $N = 1$ photon at the detector for $E = 10^8$ GeV below the highest calculated conversion probabilities.

Additionally, the combinations of energy and conversion probability fulfilling the calculated ratios can be marked in the 2D histograms plotting the conversion probability against the particle energy displayed in the previous chapter. This can be seen in Fig. 12.

On the lines marked in the diagram, the calculated ratios are exactly fulfilled and in the areas above, the ratio E/P is lower than the calculated one. As $N_\gamma \propto \frac{P}{E}$, the number of photons N_γ estimated to cross the detection are of the Pierre Auger Observatory is > 1 in these areas. They will be referred to as possible detection areas.

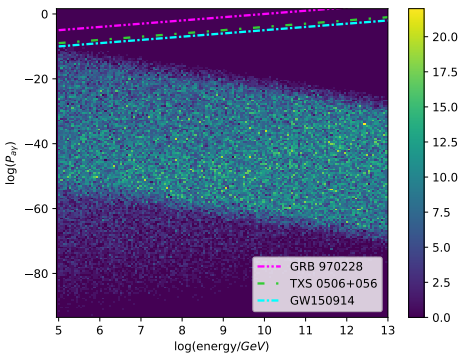

(a) Void scenario.

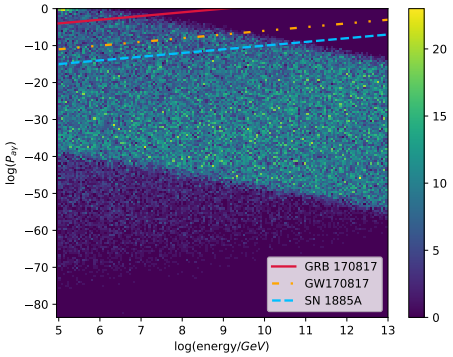

(b) Cluster scenario.

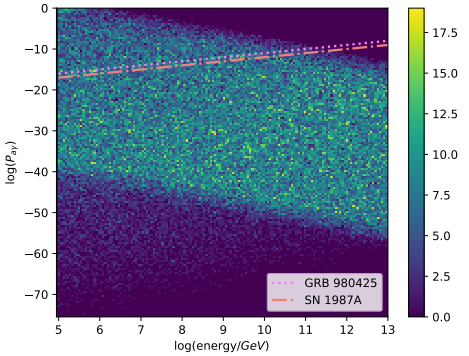

(c) Galaxy scenario.

Figure 12: 2D histogram plotting the conversion probability against the axion energy with marked E/P ratios for possible axion source candidates in the three scenarios.

It is also noticeable that above certain energy thresholds, there are no parameter combinations resulting in $P_{a\gamma}$ values in the possible detection area anymore. This energy threshold is different for the different source candidates, they are displayed in Tab. 5. Energies below these thresholds will be referred to as possible detection energies. It is noticeable that there are no possible detection energies for the source candidate GRB 970228 in the void scenario, it will be omitted in further discussions.

Events	energy threshold$E$ [GeV]
GW150914	10^5
TXS 0506+056	10^5
GRB 170817	$10^{7.5}$
GW170817	$10^{9.5}$
SN 1885A	10^{11}
GRB 980425	$10^{11.5}$
SN 1987A	$10^{11.5}$

Table 5: Energy thresholds for each of the source candidates.

5.4 Conversion probabilities and photon numbers for specific source candidates

Now conversion probabilities are calculated for each of the source candidates separately. The magnetic field strength and the electron density will be set to representative values for each of the scenarios to reduce the number of parameters. The magnetic field strength will be set to $B = 10^{-6}$ μG [51], $B = 1$ μG [41] and $B = 15$ μG for the void, cluster and Galaxy scenarios respectively, the electron density will be set to $n_e = 10^{-9}$ cm^{-3} for all of the scenarios [49]. Additionally the luminosity distance of each of the source candidates will be used. Again the number of domains is set to $N = \frac{z}{s} = 100$ but for better comparability the same set of random angles is used for the calculation of each parameter set. Now the only variable parameters are the axion mass and coupling strength as well as the energy. For each of the source candidates three energy values are chosen between $E = 10^5$ GeV and the energy thresholds given in Tab. 5 in order to probe the range of possible detection energies. For the two source candidates in the void scenario an exception is made. As the energy threshold is $E = 10^5$ GeV for GW150914 and TXS 0506+056, there is only one energy value. The axion mass and coupling strength are varied in the same ranges as before but it is no longer necessary to generate random values for these two parameters. Instead there are 100×100 equally distributed data points. For each source candidates the conversion probability is calculated as a function of axion mass and coupling strength. As there are three values chosen for the energy, this results in three sets of conversion probabilities.

As there are now only two variable parameters left, it is also possible to display these parameters on the x- and y-axis of a plot while displaying the conversion probability on the colour axis. Such plots can be seen in Fig. 13 for the source candidate GW170817 and particle energies of $E = 10^5$ GeV and $E = 10^{9.5}$ GeV. Compared to the plots above, the y-axis is shifted to higher values of the coupling strength. The conversion probability required for $N_\gamma = 1$ photon to cross the Pierre Auger Observatory is marked. Parameter combinations in the top-left corner of the plot separated by the contour lines result in conversion probabilities in the possible detection area or in other words, for these parameter combinations $N_\gamma \geq 1$ photons are expected at the Pierre Auger Observatory.

The irregularities seen in Fig. 13 occur due to the sine term in the conversion probability (equations 47 and 70) which drops to zero for certain parameter combinations of axion mass and coupling strength due to the argument of the sine approaching multiples of π.

These plots can be used to obtain threshold values for the axion mass and coupling strength. For each energy value there is a threshold for the axion mass and coupling strength above or below which the number of photons reaching the Pierre Auger Observatory is $N \geq 1$. For the source candidate GW170817 and an energy of $E = 10^5$ GeV (Fig. 13a), a coupling strength $g_{a\gamma} \geq 10^{-7} \times 10^{-11}$ GeV^{-1} and an axion mass $m_a \leq 10^{1.5}$ neV result in conversion probabilities in the possible detection area. For the higher energy of $E = 10^{9.5}$ GeV (Fig. 13b) a coupling strength of $g_{a\gamma} \geq 10^{-11}$ GeV^{-1} and a mass of $m_a \leq 10^4$ neV are required for one photon to cross the detector at the Pierre Auger Observatory. Similar plots can be made for each of the source candidates, they can be found in Appendix B. The constraints on axion

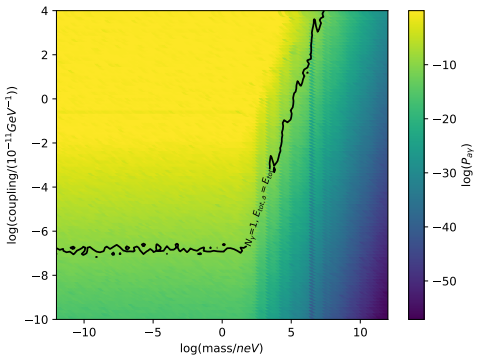

(a) Coupling strength plotted against axion mass with the conversion probability on the colour axis for axion energy $E = 10^5$ GeV.

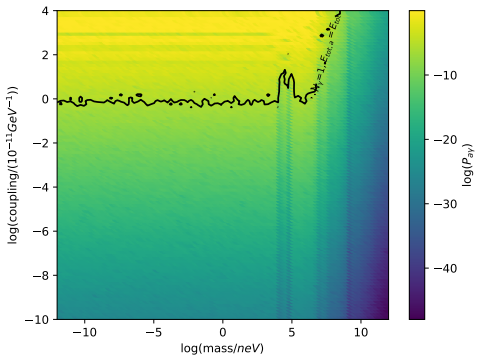

(b) Coupling strength plotted against axion mass with the conversion probability on the colour axis for axion energy $E = 10^{9.5}$ GeV.

Figure 13: Conversion probability plotted on the colour axis against the coupling strength and axion mass with marked probabilities required for $N = 1$ photons to cross the detector for the source candidate GW170817 assuming $E_{\mathrm{tot,a}} = E_{\mathrm{tot}}$.

mass and coupling strength for all of the source candidates extracted from the plots are listed in Tab. 6.

Events	energy range E [GeV]	coupling strength $g_{a\gamma}$ [10^{-11} GeV]	axion mass m_a [neV]
GW150914	10^5	$> 10^{-1}$	$< 10^{1.5}$
TXS 0506+056	10^5	$> 10^{0}$	$< 10^{1.5}$
GRB 170817	10^5 $10^{7.5}$	$> 10^{-4}$ $> 10^{0}$	$< 10^{1.5}$ $< 10^{3}$
GW170817	10^5 $10^{9.5}$	$> 10^{-7}$ $> 10^{0}$	$< 10^{1.5}$ $< 10^{4}$
SN 1885A	10^5 10^{11}	$> 10^{-7.5}$ $> 10^{0.5}$	$< 10^{2.5}$ $< 10^{6}$
GRB 980425	10^5 $10^{11.5}$	$> 10^{-7.5}$ $> 10^{1}$	$< 10^{3.5}$ $< 10^{8.5}$
SN 1987A	10^5 $10^{11.5}$	$> 10^{-9}$ $> 10^{0}$	$< 10^{3}$ $< 10^{6.5}$

Table 6: Axion mass and coupling strength required for $N_\gamma \geq 1$ photon to reach the Pierre Auger Observatory at specific particle energies for the different source candidates.

For further research the focus will be on the source candidate GW170817. So far these calculations were made under the assumption that the total emitted energy of a source candidate was emitted solely in the form of axions or in other words, the axion emission energy was assumed to be 100% of the total emitted energy. This is of

course highly unlikely. In Fig. 14a the conversion probabilities resulting in $N_\gamma \geq 1$ at the Pierre Auger Observatory are marked for the cases of the axion emission energy $E_{\mathrm{tot,a}}$ being 100%, 1% and 0.01% of the total emitted energy E_{tot}. Here the axis range has been shifted again to focus to the contour lines. As the effects of the sine term impair the readability of this plot, the lines have been smoothed out by hand to highlight the relevant regions. Additionally only 50×50 data points have been used for the edited plot. The smoothed lines match the lowest contour line in the original plot to include the full possible detection area in the region in the plot marked by the smoothed contour lines. The result can be seen in Fig. 14b.

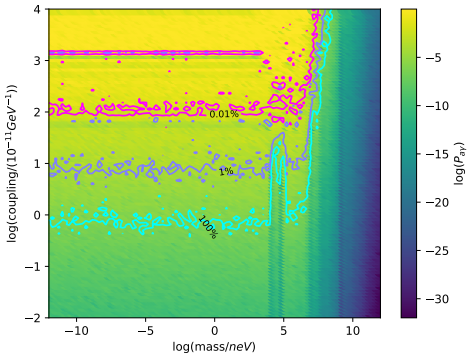

(a) Marked lines showing irregularities due to the sine term in conversion probability.

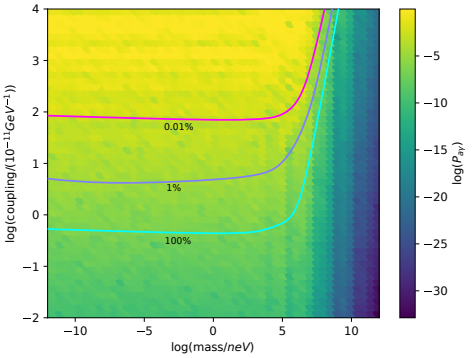

(b) Marked lines smoothed out per hand.

Figure 14: Conversion probability plotted on the colour axis against coupling strength and axion mass for GW170817 with an axion energy $E = 10^{9.5}$ GeV with multiple marked probabilities resulting in one photon crossing the detection area for the cases of the axion emission energy $E_{\mathrm{tot,a}}$ being 100%, 1% and 0.01% of the total emitted energy E_{tot}.

To discuss the number of photons crossing the detector, it is useful not to plot the conversion probability and marking thresholds for certain photon numbers but to instead plot the photon number directly against the axion mass and coupling strength. The plots for a photon number calculated via equation (71) can be seen in Fig. 15 for a particle energy $E = 10^{9.5}$ GeV. The lines mark the parameter combinations resulting in $N_\gamma = 10^{-2}$, 10^0, 10^2 and 10^4 photons crossing the Pierre Auger Observatory for an axion emission energy $E_{\mathrm{tot,a}} = E_{\mathrm{tot}}$. As before the effects occurring due to the sine term impair the readability, therefore the contour lines have been smoothed manually again. Again 50×50 data points have been used.

For this plot it was assumed again that 100% of the energy of a source candidate is emitted in the form of axions. Again, this is highly unlikely. The problem of the exact axion emission being unknown can be addressed by comparing the number of axions emitted at the source to the number of neutrinos. It can be assumed that the number of photons is similar to the number of neutrinos at the source as they both result from the decay of pions. Additionally the magnetic field close to the source candidate is most likely extremely high. For conversions of photons into axions close to the source, a simplified version of equation (47) can be used to calculate the probability of conversion. The dependence on the magnetic field strength is different

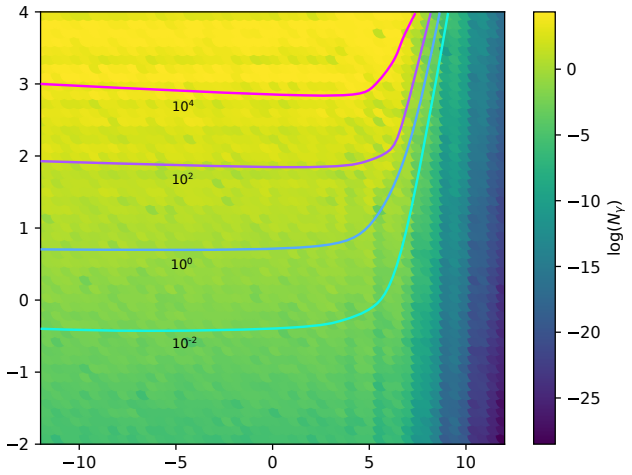

Figure 15: Number of photons crossing the Pierre Auger Observatory plotted on the colour axis against coupling strength and axion mass for GW170817 with an axion energy $E = 10^{9.5}$ GeV with marked parameter combinations resulting in $N_\gamma = 10^{-2}$, 10^0, 10^2 and 10^4 photons crossing the detector for the case $E_{\mathrm{tot,a}} = E_{\mathrm{tot}}$.

to the one used for the calculations above and therefore high magnetic fields lead to high conversion probabilities. Therefore it can be assumed that approximately all photons convert into axions and therefore the number of axions is assumed to be similar to the number of neutrinos at the source. For simplicity the total energy emitted in the form of axions will be compared to the energy emitted in the form of neutrinos.

Constraints on the energy emitted in the form of neutrinos from GW170817 can be obtained from different experiments but as this research focuses on the search for axions via the Pierre Auger Observatory, the constraints provided by this experiment will be used. The neutrino spectral fluence was measured during a ± 500 s window around the gravitational wave signal [64]. There are constraints from the Pierre Auger Observatory above neutrino energies of $E \approx 10^7$ GeV. From the plot given in reference [64] upper limits on the spectral fluence can be extracted. For energies in the ranges $E = 10^7 - 10^8$ GeV and $E = 10^{10} - 10^{11}$ GeV a limit on the spectral fluence of $< 10^1$ GeV/cm^2 per neutrino flavour can be read off, for energies in the ranges $E = 10^8 - 10^9$ GeV and $E = 10^9 - 10^{10}$ GeV the upper limit is $< 10^0$ GeV/cm^2 per flavour. To make calculations more compact, a spectral fluence of $< 10^0$ GeV/cm^2 will be used for further calculations. With three neutrino flavours, an upper limit on the total spectral fluence of $< 3 \cdot 10^0$ GeV/cm^2 can be estimated. Additionally it can be assumed that neutrinos are emitted homogeneously from the source which leads to a uniform distribution over a sphere with a radius of 39472 kpc. This radius corresponds to the distance between earth and the source of GW170817 [53]. From this a total energy emitted in the form of neutrinos can be estimated to be $E_{\mathrm{tot},\nu} \lesssim 5.6 \cdot 10^{53}$ GeV which corresponds to roughly 1.2% of the total emitted energy of the

source. The axion emission energy will be rounded to $E_{\mathrm{tot,a}} = 0.01 E_{\mathrm{tot}} = 4.5 \cdot 10^{53}$ GeV. This value will be used for further calculations.

5.5 Discussing axions with energy spectra

Additionally to the energy of a source candidate being not emitted purely in the form of axions, not all particles are emitted with one fixed energy but rather follow an energy spectrum. For further calculations an E^{-2}-spectrum will be assumed which means $\frac{dN_a}{dE} \propto E^{-2}$ or rather $\frac{dN_a}{dE} = \mathcal{N} E^{-2}$ where $\frac{dN_a}{dE}$ is the differential flux of axions at energy E emitted at the source and $\mathcal{N}$ is a normalisation factor. It can be calculated by rewriting $N_a = \frac{E_{\mathrm{tot,a}}}{E}$ and therefore $\frac{dN_a}{dE} = \frac{1}{E}\frac{dE_{\mathrm{tot,a}}}{dE} = \mathcal{N} E^{-2}$. From this

$$dE_{\mathrm{tot,a}} = \frac{dN_a}{dE} E \, dE \tag{73}$$

$$= \mathcal{N} E^{-1} \, dE \tag{74}$$

and therefore

$$\mathcal{N} = E_{\mathrm{tot,a}} \left[\int_{E_0}^{E_1} E^{-1} \, dE \right]^{-1} \tag{75}$$

can be obtained. Here $E_{\mathrm{tot,a}}$ is assumed to be known and E_0 and E_1 are the lower and upper ends of the energy spectrum which can be chosen freely. As all scales including the energy scale have been set logarithmically in all calculations, E will be substituted with $10^{E_{exp}}$. This results in

$$\mathcal{N} = E_{\mathrm{tot,a}} \left[\int_{\log(E_0)}^{\log(E_1)} 10^{-E_{exp}} 10^{E_{exp}} \ln(10) \, dE_{exp} \right]^{-1} \tag{76}$$

$$= \frac{E_{\mathrm{tot,a}}}{\ln(10) \log(E_1/E_0)} \tag{77}$$

where $\log(x)$ is used for $\log_{10}(x)$. With the normalisation factor the number of photons crossing the detector at the Pierre Auger Observatory can be calculated. Equation 71 can be rewritten as

$$dN_\gamma = P_{a\gamma}(E, g_{a\gamma}, m_a) dN_a \cdot \frac{3000 \text{ km}^2}{4\pi R^2} \tag{78}$$

$$= P_{a\gamma}(E, g_{a\gamma}, m_a) \frac{dN_a}{dE} \cdot \frac{3000 \text{ km}^2}{4\pi R^2} dE. \tag{79}$$

Then $\frac{dN_a}{dE}$ is replaced with $\mathcal{N} E^{-2} = \frac{E_{\mathrm{tot,a}}}{\ln(10)\log(E_1/E_0)} E^{-2}$ and the fraction $\frac{3000 \text{ km}^2}{4\pi R^2}$ will be referred to as q as it is constant for a specific source candidate. The number of photons crossing the detector can then be rewritten as

$$dN_\gamma(E_{\mathrm{tot,a}}) = P_{a\gamma}(E, g_{a\gamma}, m_a) \frac{E_{\mathrm{tot,a}}}{\ln(10)\log(E_1/E_0)} E^{-2} q \, dE \tag{80}$$

$$\tag{81}$$

from which

$$N_\gamma(E_{\mathrm{tot,a}}) = \frac{E_{\mathrm{tot,a}} \cdot q}{\ln(10)\log(E_1/E_0)} \int_{E_0}^{E_1} P_{a\gamma}(E, g_{a\gamma}, m_a) E^{-2}\, dE \tag{82}$$

can be obtained.

Applying the same substitution as above results in

$$N_\gamma(E_{\mathrm{tot,a}}) = \frac{E_{\mathrm{tot,a}} \cdot q}{\ln(10)\log(E_1/E_0)} \int_{\log(E_0)}^{\log(E_1)} P_{a\gamma}(10^{E_{exp}}, g_{a\gamma}, m_a) 10^{-E_{exp}} \ln(10)\, dE_{exp} \tag{83}$$

$$= \frac{E_{\mathrm{tot,a}} \cdot q}{\log(E_1/E_0)} \int_{\log(E_0)}^{\log(E_1)} P_{a\gamma}(10^{E_{exp}}, g_{a\gamma}, m_a) 10^{-E_{exp}}\, dE_{exp}. \tag{84}$$

As gammaALPs can only provide conversion probabilities for specific energy values and the integral of $P_{a\gamma}$ cannot be easily solved analytically, it is approximated by a Riemann sum resulting in

$$N_\gamma(E_{\mathrm{tot,a}}) = \frac{E_{\mathrm{tot,a}} \cdot q}{\log(E_1/E_0)} \sum_{i=1}^{K} P_{a\gamma}(10^{E_{exp,i}}, g_{a\gamma}, m_a) 10^{-E_{exp,i}} \Delta_{E_{exp}} \tag{85}$$

with

$$\Delta_{E_{exp}} = \frac{E_{exp,1} - E_{exp,0}}{N} = \frac{\log(E_1/E_0)}{K}. \tag{86}$$

This finally leads to

$$N_\gamma(E_{\mathrm{tot,a}}) = E_{\mathrm{tot,a}} \cdot \frac{q}{K} \sum_{i=1}^{K} P_{a\gamma}(10^{E_{exp,i}}, g_{a\gamma}, m_a) 10^{-E_{exp,i}} \tag{87}$$

$$= E_{\mathrm{tot,a}} \cdot \frac{q}{N} \sum_{i=1}^{K} P_{a\gamma}(E_i, g_{a\gamma}, m_a) E_i^{-1} \tag{88}$$

where the E_i are distributed on a logarithmic scale. For the following calculations $K = 100$ is chosen.

Taking into account the assumption that roughly 1% of the total energy is emitted in the form of axions and considering particle energies distributed over a E^{-2}-spectrum, the photon number crossing the detector at the Pierre Observatory can be calculated and plotted against axion mass and coupling strength again. This can be seen in Fig. 16 for the source candidate GW170817 and the energy spectrum $E = 10^9 - 10^{10}$ GeV. Again, the range of the coupling strength has been shifted to focus on the contour lines. The effects from the sine term are mostly washed out here due to the energies being distributed over the spectrum.

Until now $N_\gamma = 1$ was used as a significant photon number but it might be more sensible to use $N_\gamma = 10^{-2}$ which corresponds to a 1% chance of one photon crossing the Pierre Auger Observatory. A coupling strength of $g_{a\gamma,\mathrm{min}} = 10^{-0.3} \cdot 10^{-11}$ GeV^{-1} is required for $N_\gamma = 10^{-2}$ photons to cross the Pierre Auger Observatory for the given energy range. It is noticeable that the axion mass has little effect on the

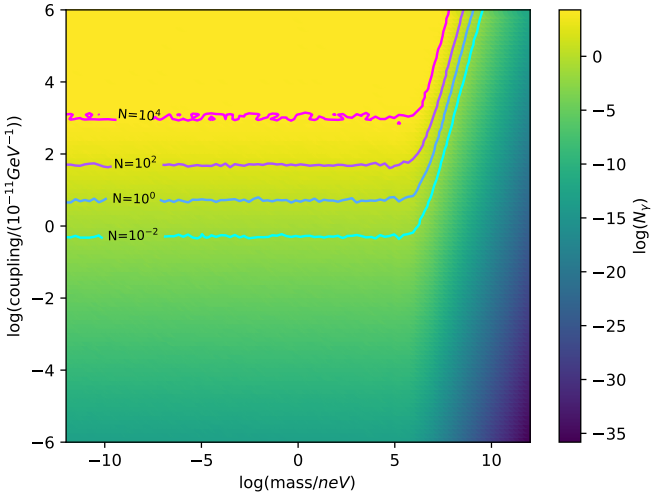

Figure 16: Photon number calculated with equation (88) plotted on the colour axis against coupling strength and axion mass with contour lines marking $N_\gamma = 0.01$, 1 and 100 photons crossing the detector for the source candidate GW170817 assuming $E_{\mathrm{tot,a}} = 0.01 E_{\mathrm{tot}}$ and $E = 10^9 - 10^{10}$ GeV.

photon number below a certain axion mass threshold which is $m_{a,th} \approx 10^6$ neV for this specific parameter constellation. Similar plots can be produced for different energy ranges, they can be found in Appendix C. The threshold axion mass and minimum coupling strength for different energy ranges are displayed in Tab. 7 as well as in Fig. 17.

energy range E [GeV]	axion mass threshold $m_{a,th}$ [neV]	minimum coupling strength $g_{a\gamma,\mathrm{min}}$ [10^{-11} GeV]
$10^{10} - 10^{11}$	$\leq 10^7$	$\geq 10^{1.2}$
$10^9 - 10^{10}$	$\leq 10^6$	$\geq 10^{-0.3}$
$10^8 - 10^9$	$\leq 10^5$	$\geq 10^{-1.8}$
$10^7 - 10^8$	$\leq 10^4$	$\geq 10^{-3.2}$
$10^6 - 10^7$	$\leq 10^3$	$\geq 10^{-4.7}$

Table 7: Axion mass thresholds below which conversion probability and photon number are constant and coupling strength required for the production of $N_\gamma \geq 10^{-2}$ photons for specific energy ranges.

The shapes of the actual curves seen in Fig. 16 are simplified for Fig. 17. It is noticeable that for the highest energy range the parameter combinations resulting in a significant amount of photons are already excluded by experiments. For lower energy ranges the necessary coupling strength decreases.

As the axion mass has no effect on the photon number below an energy-dependent threshold it is reasonable to keep it constant while varying the coupling strength and energy range. As even for the lowest energy ranges discussed here the axion mass threshold is at $m_{\mathrm{a,th}} = 10^3$ neV the axion mass will be set to $m = 10^0$ neV for

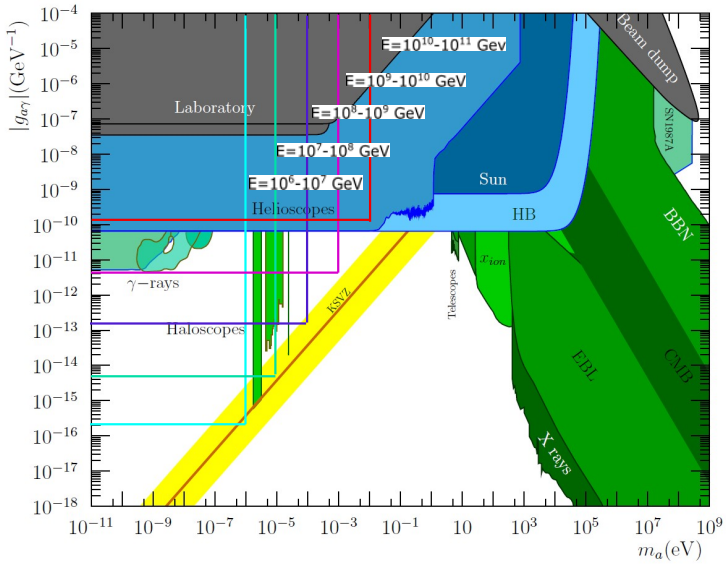

Figure 17: Coupling strength required to produce $N_\gamma \geq 10^{-2}$ photons for the source candidate GW170817 for different particle energy ranges.

the following calculations. The coupling strength for each energy interval resulting in $N_\gamma = 10^{-2} - 10^4$ photons is displayed in Fig. 18. The energy E_0 displayed on the x-axis gives the lower end of the energy spectra which span over one magnitude each. The slight irregularities seen in this plot again stem from the sine term in the

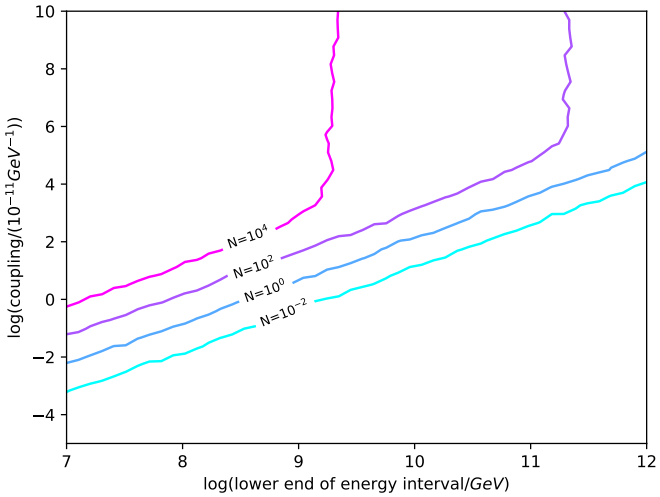

Figure 18: coupling strength resulting in $N_\gamma \geq 10^{-2} - 10^4$ for specific energy intervals for the source candidate GW170817 assuming $E_{\mathrm{tot,a}} = 0.01 E_{\mathrm{tot}}$ and $m_a = 10^0$ neV.

conversion probability given in equation (47). The sudden increases of the slope of the contour lines for $N_\gamma = 10^4$ and $N_\gamma = 10^2$ for energies of $E_0 \approx 10^{9.2}$ GeV and

$E_0 \approx 10^{11.4}$ GeV, respectively, are most likely due to a term containing the coupling strength overpowering an energy-dependent term. It is again noticeable that for lower energies, a lower coupling strength is required for the production of the same number of photons. In addition to studying the effects of the coupling strength and particle energy, it is interesting to examine the effects of the distance of a source candidate as well.

5.6 GW170817 at different distances

We will now discuss a binary neutron star merger event similar to GW170817 at different luminosity distances from earth.

For the total energy emission of the source, $E_{\text{tot}} = 4.5 \cdot 10^{55}$ GeV will be used and the axion emission energy will be set to $E_{\text{tot,a}} = 0.01 E_{\text{tot}} = 4.5 \cdot 10^{53}$ GeV. The axion mass is assumed to be constant at $m_a = 10^0$ neV as the photon number is independent of the axion mass below the threshold axion mass. The variable parameters are still the coupling strength and the energy spectrum. The same calculations as above are now performed for different luminosity distances varying between $D_L = 500$ kpc and $D_L = 10^7$ kpc.

As above, the photon number is calculated and parameter combinations resulting in an expected photon number are marked in Fig. 19.

In Fig. 17 it is noticeable that there is an upper bound on the coupling strength which is roughly $g_{a\gamma} < 10^{0.78} \cdot 10^{-11}$ GeV^{-1} for the axion mass range $m_a \approx (10^2 - 10^9)$ neV. Additionally it is important to notice that the Pierre Auger Observatory is only sensitive to photons with energies above $E = 0.2 \cdot 10^{18}$ eV $\approx 10^{8.3}$ GeV [11].

Marking this energy and the lowest possible coupling strength not excluded by other experiments in the plots of Fig. 19 makes it clear that no significant number of photons can reach the detector from sources with luminosity distances $D_L \geq 10^7$ kpc which is about a magnitude larger than the luminosity distance of the blazar TXS 0506+056.

The focus will now be on the energies in the range $E = 10^8 - 10^{11}$ GeV as these are energies detectable at the Pierre Auger Observatory. This energy range will be split into 3 different intervals $E = 10^8 - 10^9$ GeV, $E = 10^9 - 10^{10}$ GeV and $E = 10^{10} - 10^{11}$ GeV.

For each of the energy intervals the number of photons can be calculated depending on a varying coupling strength and luminosity distance. The results of the calculation can be seen in Fig. 20. Again, calculations were made with $m = 10^0$ neV. Additionally to the threshold values for the photon number, the upper bound on the coupling strength $g_{a\gamma} = 10^{0.78} \cdot 10^{-11}$ GeV^{-1} is marked with a blue horizontal line. The area in the axion mass-coupling strength parameter space in which QCD axions can exist, is marked in yellow in Fig. 17. For the threshold axion masses given in Tab. 7 the coupling strengths allowing for a QCD axion are marked in yellow in Fig. 20 as well. The ranges of coupling strength fulfilling the conditions for the QCD axion are $g_{a\gamma} = (10^{-5.4} - 10^{-3.7}) \cdot 10^{-11}$ GeV^{-1}, $g_{a\gamma} = (10^{-4.4} - 10^{-2.7}) \cdot 10^{-11}$ GeV^{-1} and $g_{a\gamma} = (10^{-3.4} - 10^{-1.7}) \cdot 10^{-11}$ GeV^{-1} for the axion masses $m = 10^3$ neV, $m = 10^4$ neV and $m = 10^5$ neV respectively. Additionally the red band marks the HB-hint region discussed in chapter 3.2.1. The irregularities seen here are again most likely due to the sine term dropping to zero.

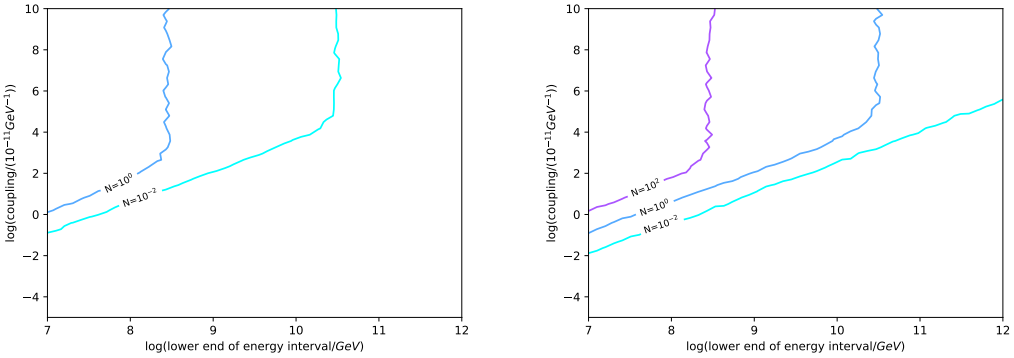

(a) $D_L = 10^7$ kpc

(b) $D_L = 10^6$ kpc

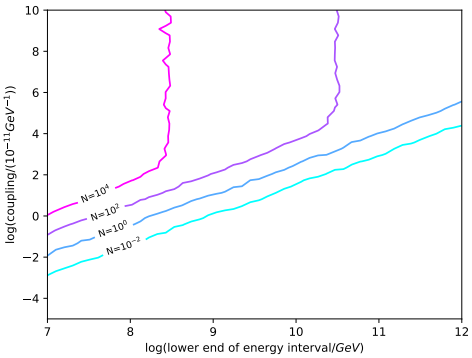

(c) $D_L = 5 \cdot 10^5$ kpc

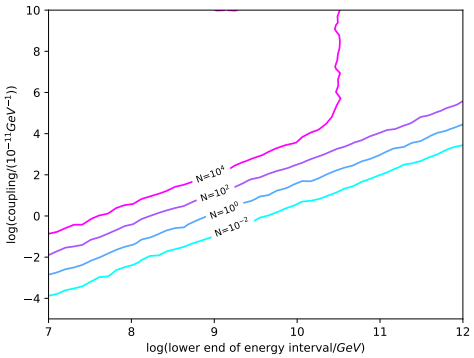

(d) $D_L = 10^4$ kpc

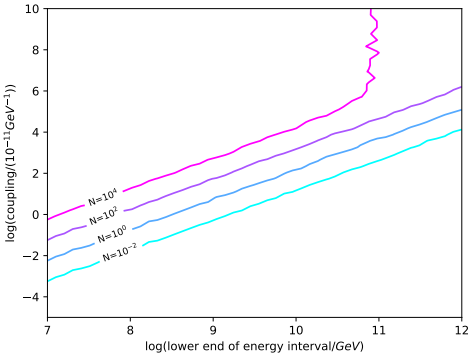

(e) $D_L = 5 \cdot 10^3$ kpc

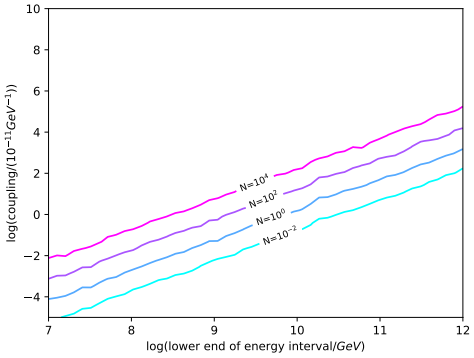

(f) $D_L = 5 \cdot 10^2$ kpc

Figure 19: Parameter combinations of coupling strength and axion energy resulting in a threshold number of photons for different luminosity distances for a source similar to GW170817 assuming an axion emission energy of $E_{\mathrm{tot,a}} = E_{\mathrm{tot,GW170817}}$.

One important observation from the plots displayed in Fig. 20 is that for lower energy ranges it is more likely to detect a higher number of photons converted from axions. For the energy range $E = (10^{10} - 10^{11})$ GeV it is possible to detect $N_\gamma \geq 10^{-2}$

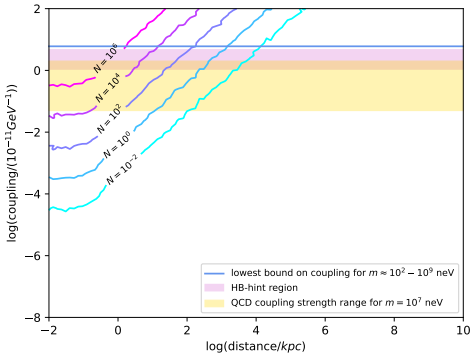

(a) $E = 10^{10} - 10^{11}$ GeV.

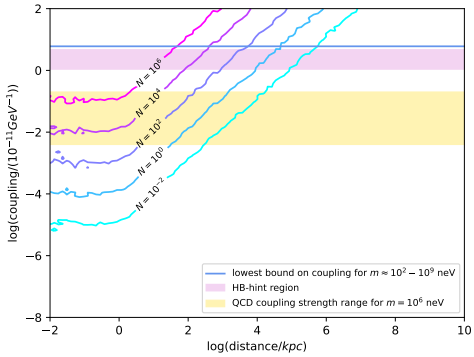

(b) $E = 10^9 - 10^{10}$ GeV.

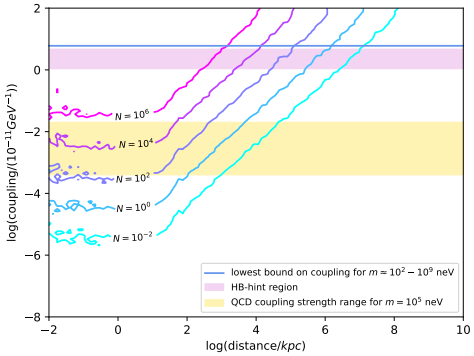

(c) $E = 10^8 - 10^9$ GeV.

Figure 20: Parameter combinations of coupling strength and luminosity distances resulting in a threshold number of photons for different energy ranges assuming a source similar to GW170817 with $E_{\mathrm{tot,a}} = 0.01 E_{\mathrm{tot,\ GW170817}}$. The horizontal lines and bars mark the upper limit on the coupling strength, the HB-hint region and the QCD axion coupling range.

photons for distances of $D_L \lesssim 10^{4.1}$ kpc which is similar to the distance of the source of GW170817. For the energy ranges $E = (10^9 - 10^{10})$ GeV and $E = (10^8 - 10^9)$ GeV the lowest luminosity distances where $N_\gamma \geq 10^{-2}$ photons could still be expected at the Pierre Auger Observatory are $D_L \lesssim 10^{5.6}$ kpc and $D_L \lesssim 10^{7.1}$ kpc respectively which is considerably higher. The latter roughly corresponds to the maximum distance determined in Fig. 19. The maximum distances from which axions in the HB-hint region could be detected are just about $0.1 - 0.2$ magnitudes lower than the maximum distances for detection of general axions. In comparison, the distances from which QCD axions could be detected are significantly lower. For the highest energy range $E = (10^{10} - 10^{11})$ GeV the distance for the detection of QCD axions is $D_L \lesssim 10^{3.7}$ kpc which corresponds to distances of sources just beyond the Local Group. The distance for the energy ranges $E = (10^9 - 10^{10})$ GeV and $E = (10^8 - 10^9)$ GeV are $D_L \lesssim 10^{4.2}$ kpc and $D_L \lesssim 10^{4.6}$ kpc, respectively. The latter is comparable to the distance of GW170817.

The same calculations can be performed for lower energies even though they are not

accessible by the Pierre Auger Observatory yet. The plots are displayed in Fig. 21.

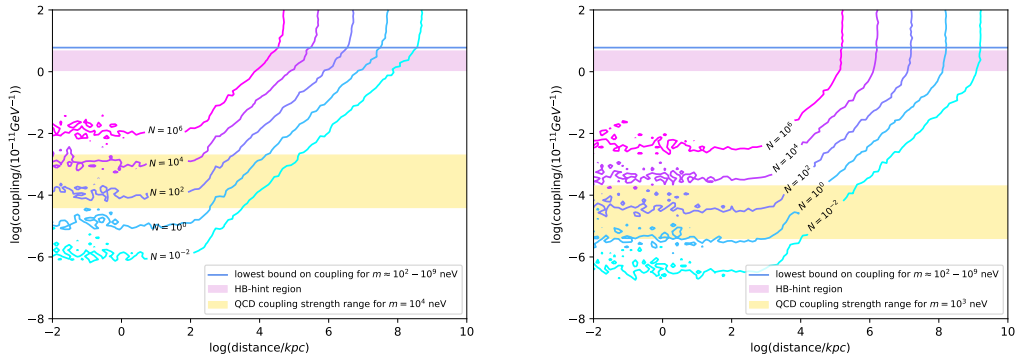

(a) $E = 10^7 - 10^8$ GeV. (b) $E = 10^6 - 10^7$ GeV.

Figure 21: Parameter combinations of coupling strength and luminosity distances resulting in a threshold number of photons for different energy ranges assuming a source similar to GW170817 with $E_{\mathrm{tot,a}} = 0.01 E_{\mathrm{tot,\ GW170817}}$. The horizontal lines and bars mark the upper limit on the coupling strength, the HB-hint region and the QCD axion coupling range.

Decreasing the energy range to $E = 10^7 - 10^8$ GeV could provide the means to detect photons from sources as distant as $D_L \lesssim 10^{8.5}$ kpc. Decreasing the energy range even further to $E = 10^6 - 10^7$ GeV could possibly lead to a chance to detect photons converted from axions originating from sources with luminosity distances $D_L > 10^{9.1}$ kpc. These distances exceed the limits obtained from Fig. 19 as the minimum energy has been lowered. For such distances multiple remarks are necessary. They exceed the distance of the CMB beyond which no observations can be made. Therefore assumptions about sources beyond this distance are rather speculative. Additionally, particles from such distances would have been emitted in the early stages of the universe where the kind of sources discussed above might not have existed yet. The values given here are meant to illustrate the functional behaviour of the analysed parameters.

The distances below which the threshold coupling strength $g_{a\gamma} \leq 10^{0.78} \cdot 10^{-11}$ GeV^{-1} results in $N_\gamma \geq 10^{-2}$ photons as well as distance below which axions with coupling strength in the HB-hint region could be detected are listed in Tab. 8 for all of the energy ranges discussed above.

The distances from which the detection of QCD axions are possible are given in Tab. 9. The energy dependent axion mass thresholds first mentioned in table 7 are listed as well together with their corresponding coupling strength ranges for which the QCD axion conditions hold.

It is important to remember that the magnetic field strength was set to $B = 1\ \mu$G which is a typical value for galaxy clusters. For luminosity distances $D_L \gtrsim 10^4$ kpc a lower magnetic field strength and therefore a lower conversion probability are realistic. The given results are therefore rather optimistic estimates meant to describe the functional behaviour of the conversion probability and photon number. To take variations of the magnetic field into consideration, a more detailed modelling of the

energy range E [GeV]	distance threshold for $N_\gamma \geq 10^{-2}$ [kpc]	distances threshold for $N_\gamma \geq 10^{-2}$ for axions in HB-hint region [kpc]
$10^{10} - 10^{11}$	$\leq 10^{4.1}$	$\leq 10^{4}$
$10^{9} - 10^{10}$	$\leq 10^{5.6}$	$\leq 10^{5.5}$
$10^{8} - 10^{9}$	$\leq 10^{7.1}$	$\leq 10^{7}$
$10^{7} - 10^{8}$	$\leq 10^{8.5}$	$\leq 10^{8.3}$
$10^{6} - 10^{7}$	$\leq 10^{9.1}$	$\leq 10^{9.1}$

Table 8: Energy ranges and maximum luminosity distances required for the detection of $N_\gamma \geq 10^{-2}$ photons as well as maximum luminosity distances required for the detection of $N_\gamma \geq 10^{-2}$ photons for axions with couplings in the HB-hint region for photons in energy ranges detectable by the Pierre Auger Observatory and for photons with lower energies.

energy range E [GeV]	axion mass threshold m_a [neV]	QCD coupling strength range $g_{a\gamma}$ [10^{-11} GeV]	distances threshold for $N_\gamma \geq 10^{-2}$ for axions in QCD range [kpc]
$10^{10} - 10^{11}$	$\leq 10^{7}$	$10^{-1.4} - 10^{0.3}$	$\leq 10^{3.7}$
$10^{9} - 10^{10}$	$\leq 10^{6}$	$10^{-2.4} - 10^{-0.7}$	$\leq 10^{4.2}$
$10^{8} - 10^{9}$	$\leq 10^{5}$	$10^{-3.4} - 10^{-1.7}$	$\leq 10^{4.6}$
$10^{7} - 10^{8}$	$\leq 10^{4}$	$10^{-4.4} - 10^{-2.7}$	$\leq 10^{5.1}$
$10^{6} - 10^{7}$	$\leq 10^{3}$	$10^{-5.4} - 10^{-3.7}$	$\leq 10^{5.5}$

Table 9: Energy ranges and axion mass threshold with corresponding QCD coupling ranges and maximum luminosity distances required to detect $N_\gamma \geq 10^{-2}$ photons in this range for photons in energy ranges detectable by the Pierre Auger Observatory and for photons with lower energies.

propagation scenario would be necessary. For this research these results will be considered as final results. They are displayed more comprehensively in Fig. 22. The maximum distances for each energy range discussed above are marked here in blue. Additionally the maximum distances for coupling strengths in the HB-hint region and in the QCD region are marked in red and yellow, respectively. The horizontal green line marks the lowest energy $E \approx 10^{8.3}$ GeV currently detectable at the Pierre Auger Observatory. The vertical line marks the luminosity distances $D_L \gtrsim 10^4$ kpc above which these estimates become more optimistic due to the magnetic field strength being lower beyond this distance.

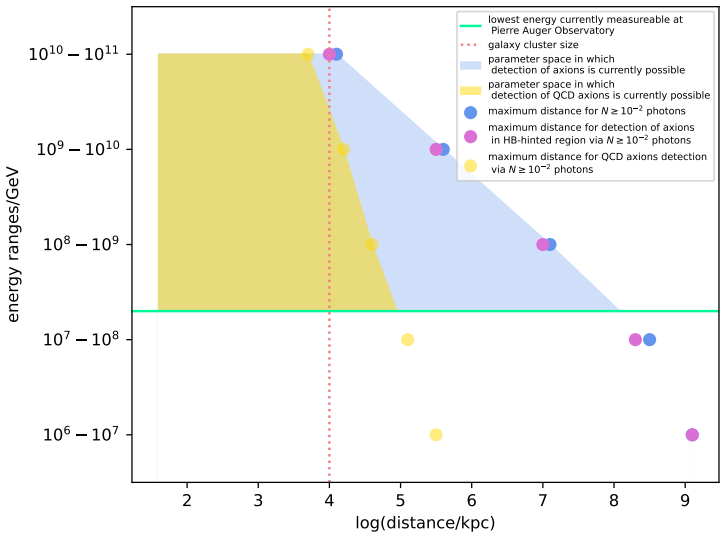

Figure 22: Energy ranges and their corresponding maximum distances for which $N_\gamma \geq 10^{-2}$ photons converted from axions, axions in the HB-hint region and QCD axions are expected at the Pierre Auger Observatory. The source is assumed to be similar to GW170817 with $E_{\mathrm{tot,a}} = 0.01 E_{\mathrm{tot,\ GW170817}}$.

6 Discussion of results

From Fig. 20 the coupling strength required for a $\geq 1\%$ chance for $N_\gamma \geq 1$ photon to cross the Pierre Auger detector at different distances and energies can be read off. These can be marked in the limits plot which is shown in Fig. 23. The lines mark the parameter combinations resulting in a $\geq 1\%$ chance of $N_\gamma = 1$ photon crossing the detector giving a guideline on the parameter ranges accessible for different source distances.

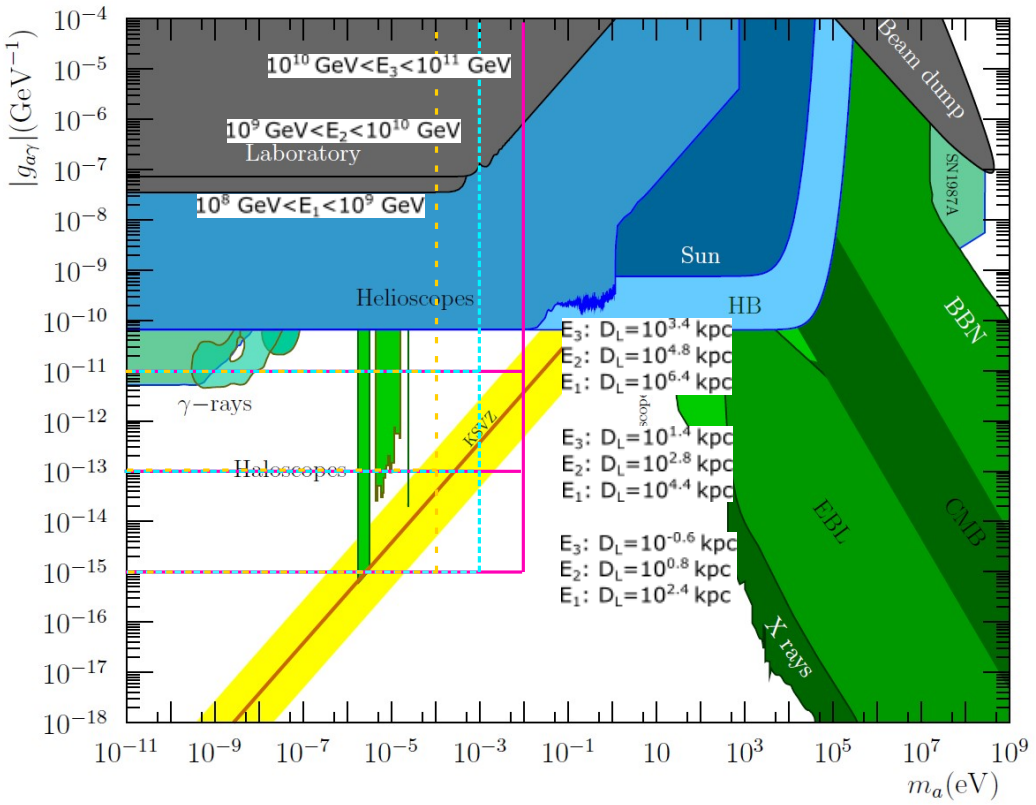

Figure 23: Maximum distances for a $> 1\%$ chance for one photon to reach the Pierre Auger Observatory at different coupling thresholds for $E_{\mathrm{tot,\,a}} = 4.5 \cdot 10^{53}$ GeV and different energy intervals. Energy ranges: magenta: 10^{10} GeV $< E_3 < 10^{11}$ GeV, cyan: 10^9 GeV $< E_2 < 10^{10}$ GeV, yellow: 10^8 GeV $< E_1 < 10^9$ GeV. Coupling strength thresholds from lowest to highest: $g_{a\gamma} = 10^{-15}$ GeV^{-1}, $g_{a\gamma} = 10^{-13}$ GeV^{-1}, $g_{a\gamma} = 10^{-11}$ GeV^{-1}.

Additionally we can take a more detailed look at Fig. 22 which displays the energy ranges and the corresponding maximum distance below which $N_\gamma \geq 1$ is expected to cross the detector at the Pierre Auger Observatory with a $> 1\%$ chance. The maximum distances for a $> 1\%$ chance for $N_\gamma \geq 1$ photon resulting from a QCD axion or an axion in the HB-hint region to cross the detector are marked as well. For the highest energy range 10^{10} GeV $< E < 10^{11}$ GeV the maximum distances of $D_L = 10^{4.1}$ is in the range of the Virgo Supercluster, for 10^9 GeV $< E < 10^{10}$ GeV the maximum distance is $D_L = 10^{5.6}$ kpc which is similar to the luminosity distance

of GW150914. For the lowest energy range 10^8 GeV $< E < 10^9$ GeV detectable by the Pierre Auger Observatory, axions from sources beyond these distances may be observed. As the maximum distance for the detection of axions in the HB-hint region is only $0.1 - 0.2$ magnitudes lower than the maximum distance for the detection of axions, it is possible to detect axions in the HB-region as well. It is however less likely but still not impossible to detect axions in the QCD range. For the highest energy 10^{10} GeV $< E < 10^{11}$ GeV the maximum distance for QCD axions is $D_L = 10^{3.7}$ kpc $= 5$ Mpc. For the lowest energy range currently measurable the maximum distance is $D_L = 10^{4.6}$ kpc ≈ 39.8 Mpc which is similar to the luminosity distance of GW170817.

By lowering the measurable energy at the Pierre Auger Observatory, the maximum detectable distance increases. Decreasing the detectable energy about one magnitude, increases the maximum distance for the measurement of a QCD axion by $0.4 - 0.6$ magnitudes depending on the specific energy range. For the measurement of an axion-like particle an extension to lower energies theoretically provides benefits as well. By lowering the energy by one magnitude, the maximum distance for the detection of axions increases by ≈ 1.5 magnitudes but as mentioned above, distances as high as 10^9 kpc are not relevant for the detection of axions anymore. But still, the plot provides a rough guideline on which sources to investigate in more detail in future searches.

6.1 Critical evaluation of results

As mentioned above, the plot becomes highly optimistic beyond the range of the Virgo Supercluster which is $D_L \approx 10^4$ kpc. For higher distances, the given estimates are rather optimistic due to the assumption of the magnetic field strength being $B = 1$ μG which is a likely value for galaxy clusters but not for the medium beyond such structures. Besides the high estimate for the magnetic field strength for distances beyond distances of $D_L \gtrsim 10^4$ kpc, the estimated magnetic field strength might be too low for lower distances due to the galactic magnetic field strength being considerably higher than the one in cluster medium. Particles from galactic sources with distances $D_L \lesssim 10^1$ kpc propagate exclusively through galactic medium and even particles from sources with distances $D_L \gtrsim 10^4$ kpc traverse galactic medium before arriving at the detector. Both of these effects have not been considered in the calculations above. A detailed analysis of magnetic fields for specific regions would potentially increase the number of photons for sources at distances $D_L \lesssim 10^4$ kpc. For particles from sources with distances $D_L \gtrsim 10^4$ kpc the discussed effect have contradicting influence on the photon number. A more detailed analysis would be needed to investigate the overall result on the photon number.

Another effect not discussed here is the interaction of photons with the CMB and the universal radio background (URB) during their propagation. This effect is not negligible especially for axions which converted into photons close to the source. Through this effect the photon number is reduced for distant sources. For such photons a reconversion into axions is possible as well even though it is less likely than the interactions with the CMB and URB.

Additionally, the area of the Pierre Auger Observatory used for the calculations is estimated to be 3000 km^2 for all energy ranges. This is an overestimation for low

energies. The full detector array is sensitive to energies $E \gtrsim 10^{18}$ eV $= 10^9$ GeV while the area which is sensitive to energies $E > 0.2 \cdot 10^{18}$ eV $\approx 10^{8.3}$ GeV is significantly smaller with an area of ≈ 27.5 km^2 [11]. As the detector area for the lowest order of magnitude is more than two magnitudes smaller than the full detector area, the expected photon number is about two magnitudes lower as well.

Lastly, the in detail analysis is only performed for sources with the same luminosity as GW170817. The total emitted energy of sources can assume values varying over several magnitudes impacting the number of photons and therefore the distance thresholds. For specific source candidates this variation has a specific and significant contribution to the result.

These corrections have partially contradicting effects. A more detailed analysis for individual source candidates would be needed to include areas of different magnetic field strength, interactions of photons with the CMB and URB as well as a sources specific luminosity in the calculation. The gammaALPs python package used here might be able to aid in a further analysis as it is possible to include magnetic fields and electron densities varying with the distance as well as the interaction of photons with the EBL but for simplicity these effects have not been taken into account yet.

7 Summary and outlook

In this thesis the possibilities to detect axions with the Pierre Auger Observatory have been discussed. The analysis of conversion probabilities and numbers of converted photons traversing the Pierre Auger Observatory indicates a detection is more likely for closer sources but even sources with distances in the Mpc and low Gpc scale are not out of the question.

One source candidate, GW170817, and similar sources with varying luminosity distances have been analysed in detail and the number of converted photons traversing the detector area has been calculated for different ranges of particle energy. A guideline is provided to assess which sources are worthwhile to examine in detail in future axion searches. It was clear that the probability of detection increases with decreasing particle energies. With the current setup of the Pierre Auger Observatory, which can measure energies above $E \approx 2 \cdot 10^8$ GeV, binary neutron star mergers similar to GW170817 with distances up to the megaparsec and gigaparsec scale are worthwhile to investigate in more detail. This estimation might be rather optimistic as there are several effects not considered in this calculation but it does provide a guideline for future searches. Further research is needed to take into account additionally contributing effects discussed above. This would lead to more accurate estimations of conversion probabilities, photon numbers and probabilities of detection.

8 Appendices

Appendix A

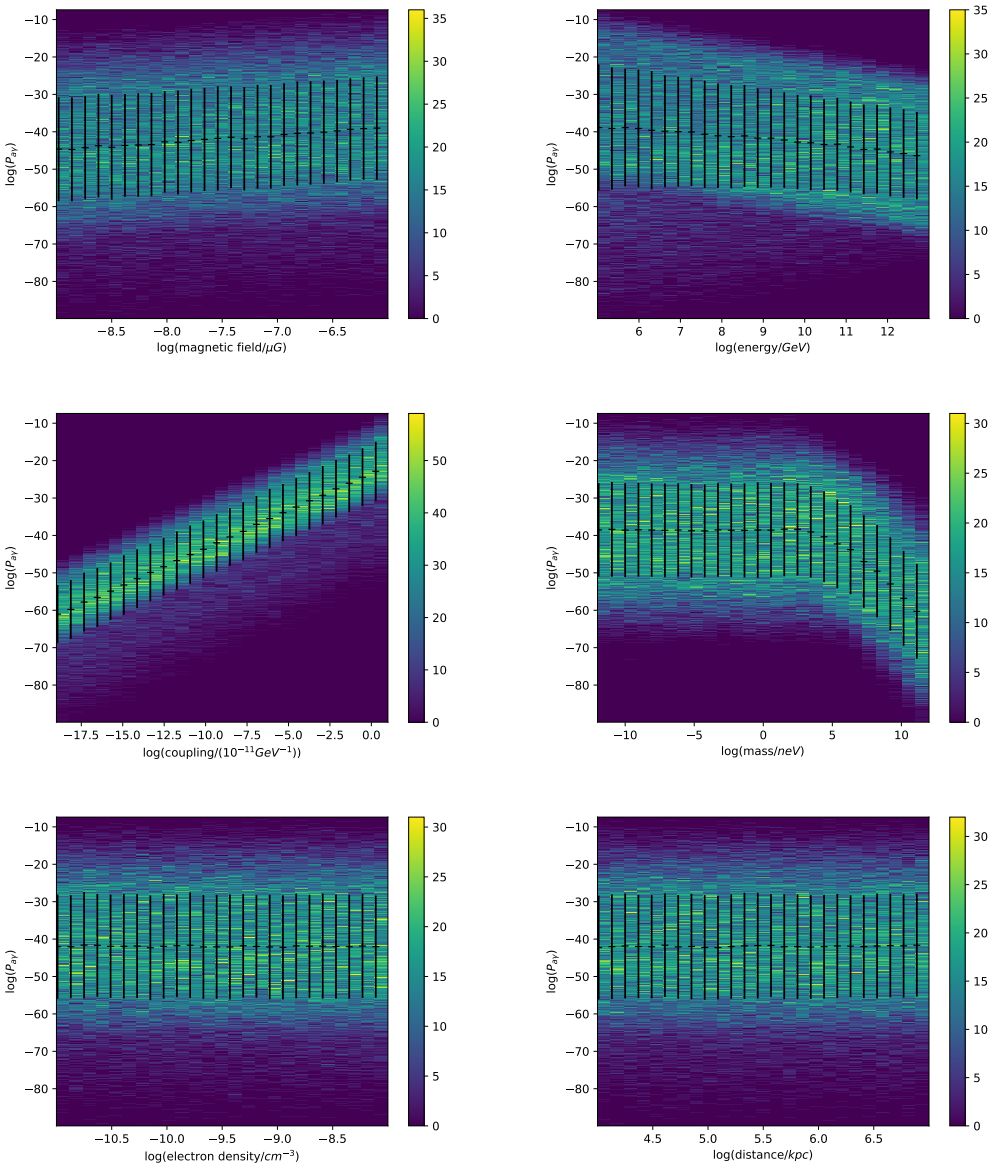

Figure 24: 2D histograms for a source located in a void plotting the conversion probability against (from top left to bottom right) magnetic field strength, axion energy, coupling strength, axion mass, electron density, distance.

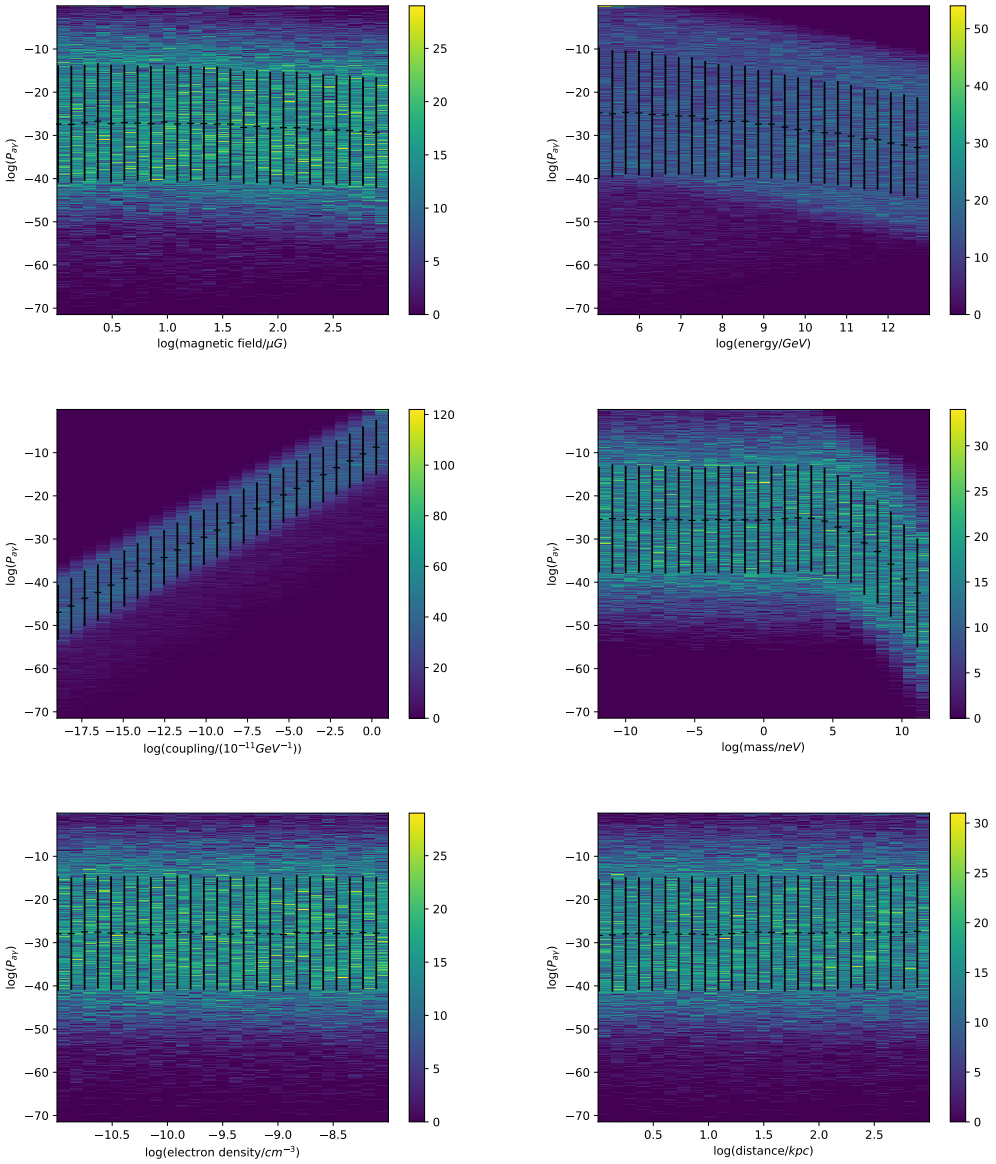

Figure 25: 2D histograms for a source located in a galactic range assuming a low electron density plotting the conversion probability against (from top left to bottom right) magnetic field strength, axion energy, coupling strength, axion mass, electron density, distance.

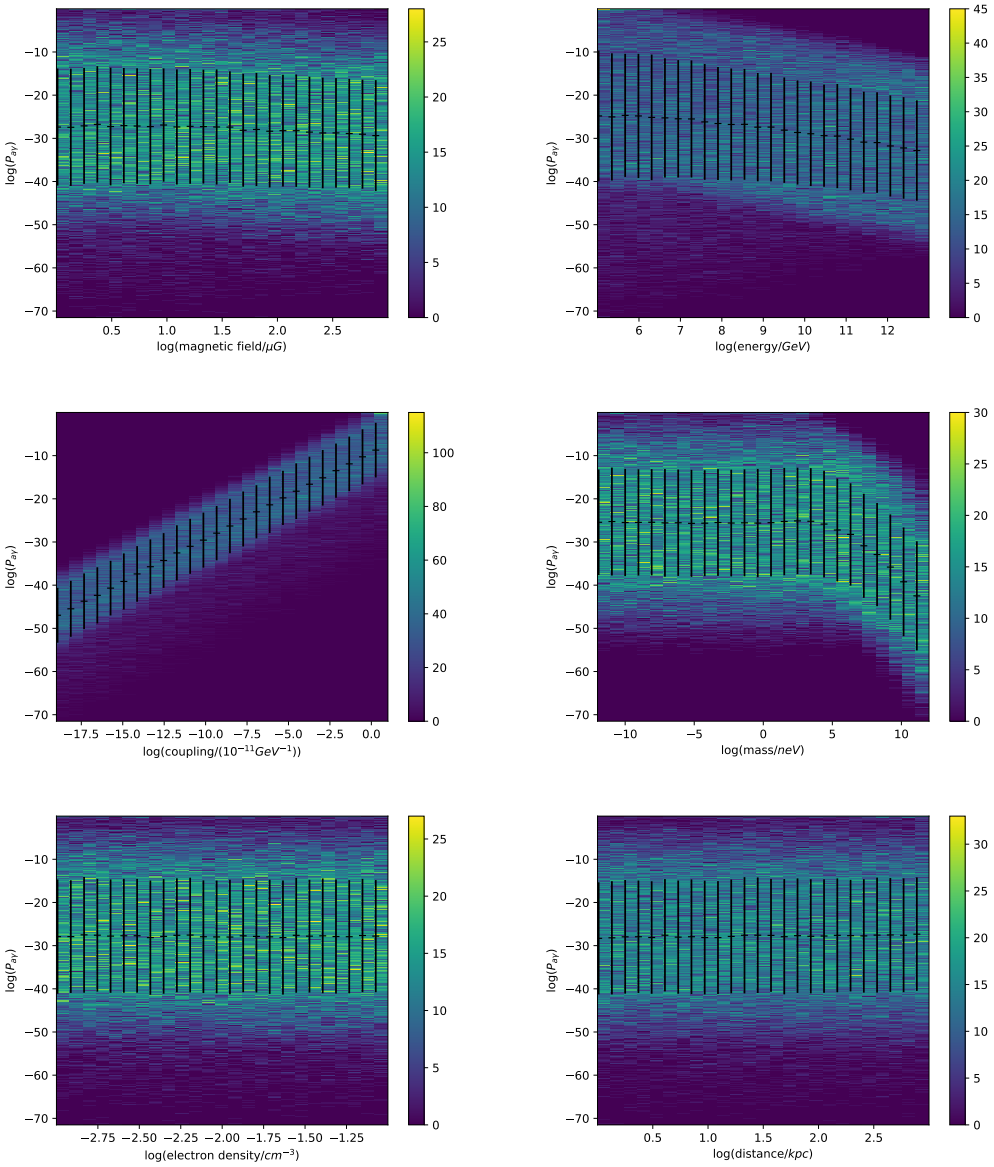

Figure 26: 2D histograms for a source located in a galactic range assuming a high electron density plotting the conversion probability against (from top left to bottom right) magnetic field strength, axion energy, coupling strength, axion mass, electron density, distance.

Appendix B

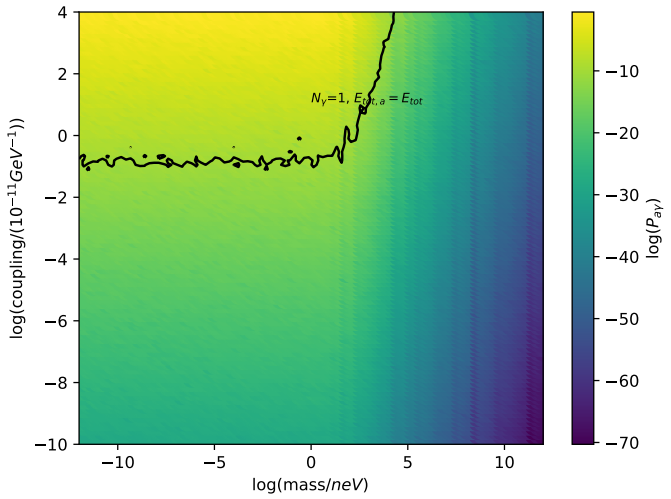

Figure 27: Conversion probability plotted on the colour axis against the coupling strength and axion mass with marked probabilities required for $N = 1$ photons to cross the detector for the source candidate GW150914 assuming an axion energy $E = 10^5$ GeV and $E_{\mathrm{tot,a}} = E_{\mathrm{tot}}$.

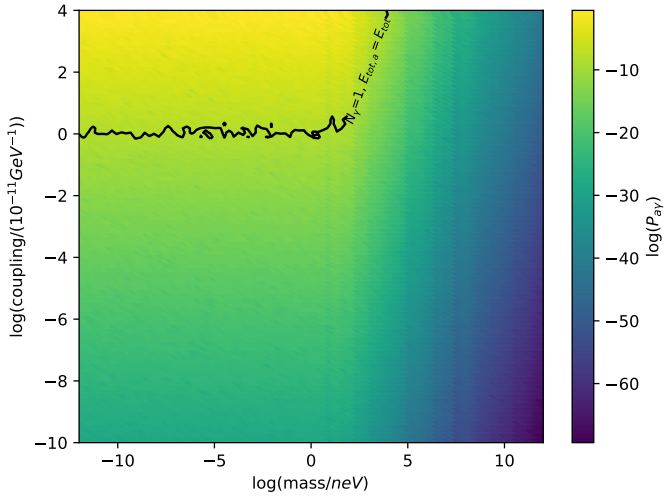

Figure 28: Conversion probability plotted on the colour axis against the coupling strength and axion mass with marked probabilities required for $N = 1$ photons to cross the detector for the source candidate TXS 0506+056 assuming an axion energy $E = 10^5$ GeV and $E_{\mathrm{tot,a}} = E_{\mathrm{tot}}$.

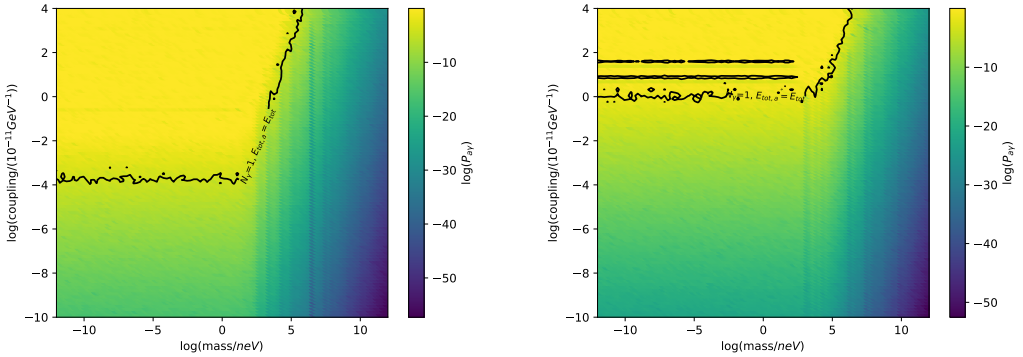

(a) Coupling strength plotted against axion mass with the conversion probability on the colour axis for axion energy $E = 10^5$ GeV.

(b) Coupling strength plotted against axion mass with the conversion probability on the colour axis for axion energy $E = 10^{7.5}$ GeV.

Figure 29: Conversion probability plotted on the colour axis against the coupling strength and axion mass with marked probabilities required for $N = 1$ photons to cross the detector for the source candidate GRB 170817 assuming $E_{\text{tot,a}} = E_{\text{tot}}$.

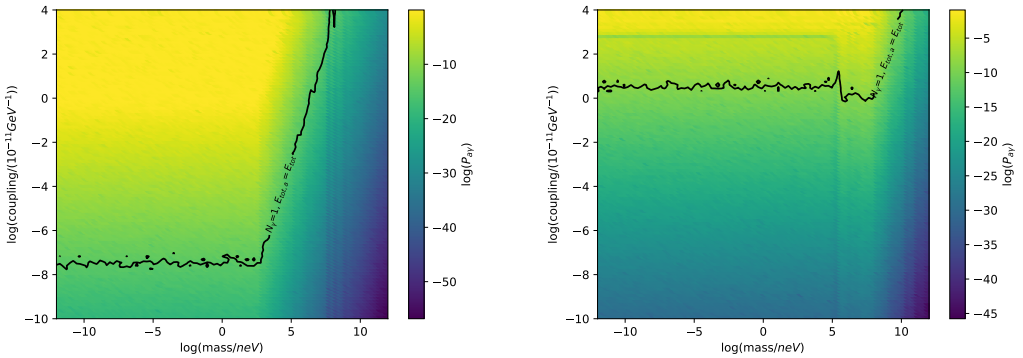

(a) Coupling strength plotted against axion mass with the conversion probability on the colour axis for axion energy $E = 10^5$ GeV.

(b) Coupling strength plotted against axion mass with the conversion probability on the colour axis for axion energy $E = 10^{11}$ GeV.

Figure 30: Conversion probability plotted on the colour axis against the coupling strength and axion mass with marked probabilities required for $N = 1$ photons to cross the detector for the source candidate SN 1885A assuming $E_{\text{tot,a}} = E_{\text{tot}}$.

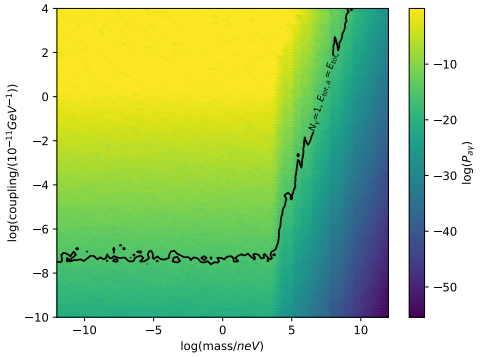

(a) Coupling strength plotted against axion mass with the conversion probability on the colour axis for axion energy $E = 10^5$ GeV.

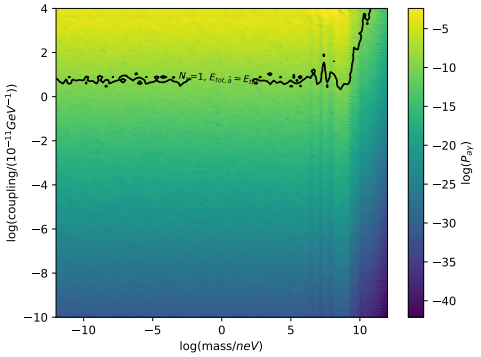

(b) Coupling strength plotted against axion mass with the conversion probability on the colour axis for axion energy $E = 10^{11.5}$ GeV.

Figure 31: Conversion probability plotted on the colour axis against the coupling strength and axion mass with marked probabilities required for $N = 1$ photons to cross the detector for the source candidate GRB 980425 assuming $E_{\mathrm{tot,a}} = E_{\mathrm{tot}}$.

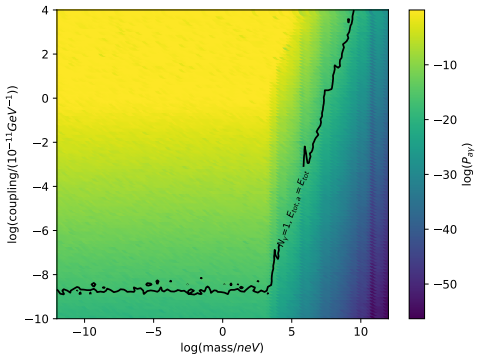

(a) Coupling strength plotted against axion mass with the conversion probability on the colour axis for axion energy $E = 10^5$ GeV.

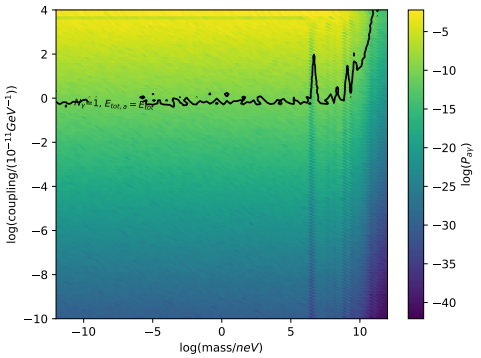

(b) Coupling strength plotted against axion mass with the conversion probability on the colour axis for axion energy $E = 10^{11.5}$ GeV.

Figure 32: Conversion probability plotted on the colour axis against the coupling strength and axion mass with marked probabilities required for $N = 1$ photons to cross the detector for the source candidate SN 1987A assuming $E_{\mathrm{tot,a}} = E_{\mathrm{tot}}$.

Appendix C

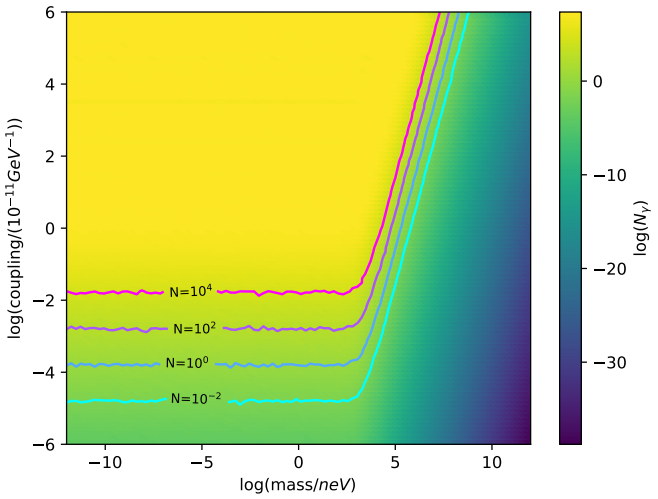

Figure 33: Photon number calculated with equation (88) plotted on the colour axis against coupling strength and axion mass with contour lines marking $N_\gamma = 0.01$, 1 and 100 photons crossing the detector for the source candidate GW170817 assuming $E_{\mathrm{tot,a}} = 0.01 E_{\mathrm{tot}}$ and $E = 10^6 - 10^7$ GeV.

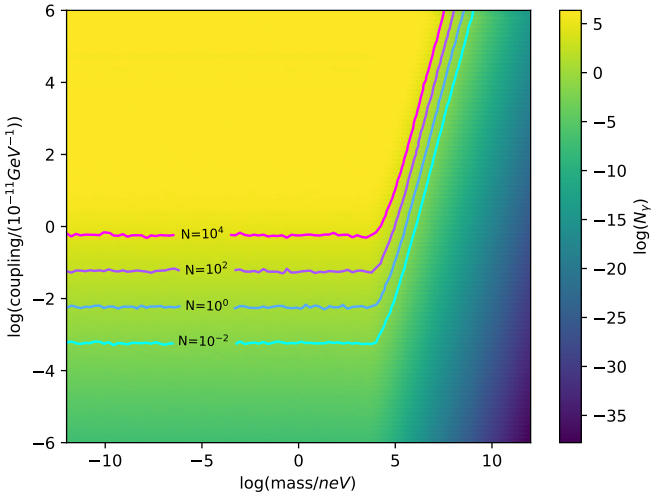

Figure 34: Photon number calculated with equation (88) plotted on the colour axis against coupling strength and axion mass with contour lines marking $N_\gamma = 0.01$, 1 and 100 photons crossing the detector for the source candidate GW170817 assuming $E_{\mathrm{tot,a}} = 0.01 E_{\mathrm{tot}}$ and $E = 10^7 - 10^8$ GeV.

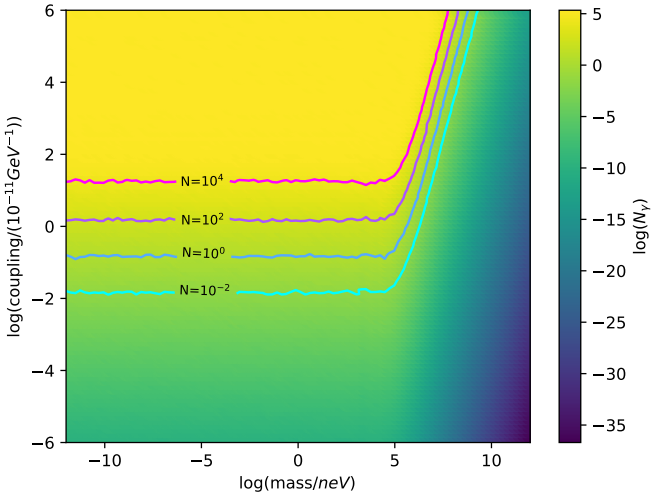

Figure 35: Photon number calculated with equation (88) plotted on the colour axis against coupling strength and axion mass with contour lines marking $N_\gamma = 0.01$, 1 and 100 photons crossing the detector for the source candidate GW170817 assuming $E_{\mathrm{tot,a}} = 0.01 E_{\mathrm{tot}}$ and $E = 10^8 - 10^9$ GeV.

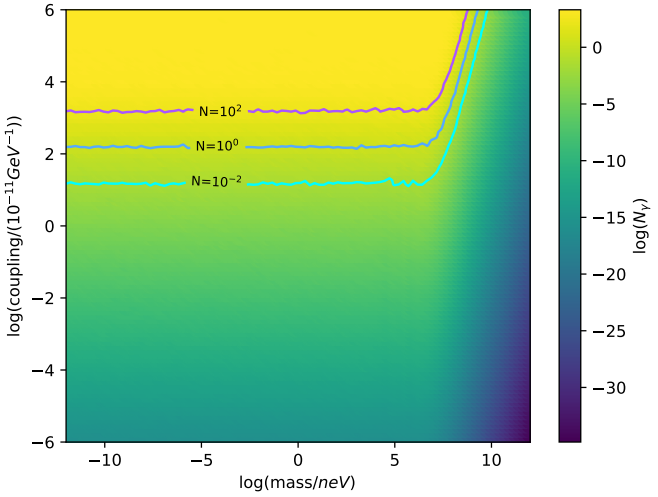

Figure 36: Photon number calculated with equation (88) plotted on the colour axis against coupling strength and axion mass with contour lines marking $N_\gamma = 0.01$, 1 and 100 photons crossing the detector for the source candidate GW170817 assuming $E_{\mathrm{tot,a}} = 0.01 E_{\mathrm{tot}}$ and $E = 10^{10} - 10^{11}$ GeV.

References

[1] Jean-Louis Tassoul, Monique Tassoul, *A Concise History of Solar and Stellar Physics*, Princeton and Oxford: Princeton University Press, 2004.

[2] R. Norris, *Dawes Review 5: Australian Aboriginal Astronomy and Navigation*, Publications of the Astronomical Society of Australia **33**, 2016. https://arxiv.org/pdf/1607.02215.pdf.

[3] Claus Grupen, *Einstieg in die Astroteilchenphysik*, Springer-Verlag 2018.

[4] https://www.auger.org/observatory/about-pierre-auger, 10.01.2022.

[5] https://upload.wikimedia.org/wikipedia/commons/0/00/Standard_Model_of_Elementary_Particles.svg, 26.01.2022.

[6] David Griffiths, *Introduction to Elementary Particles*, WllEY-VCH Verlag GmbH & Co. KGaA, 2008.

[7] A. De Angelis, G. Galanti, M. Roncadelli, *Relevance of axion-like particles for very-high-energy astrophysics*, Physical Review Letters **84**, American Physical Society 2013. https://arxiv.org/pdf/1106.1132.pdf.

[8] https://home.cern/news/news/physics/cosmic-rays-discovered-100-years-ago, 10.01.2022.

[9] https://home.cern/science/physics/cosmic-rays-particles-outer-space#:~:text=Cosmic%20rays%20are%20a%20form,Image%3A%20CERN), 10.01.2022.

[10] https://astronomy.swin.edu.au/cosmos/c/cosmic+ray+energies, 26.01.2022.

[11] The Pierre Auger Collaboration, *A Search for Photons with Energies Above* 2×10^{17} *eV Using Hybrid Data from the Low-Energy Extensions of the Pierre Auger Observatory*, The Astrophysical Journal **933**, 2, 2022. https://arxiv.org/pdf/2205.14864.pdf.

[12] Karl-Heinz Kampert et al. (The Pierre Auger Collaboration), *Multi-Messenger Physics With the Pierre Auger Observatory*, Frontiers in Astronomy and Space Sciences **6**, 2019. https://www.frontiersin.org/articles/10.3389/fspas.2019.00024/full.

[13] https://www.auger.org/observatory/auger-hybrid-detector, 10.01.2022.

[14] Helen Quinn, *The CP Puzzle in the Strong Interactions*,hep-ph/0110050 2001. https://arxiv.org/abs/hep-ph/0110050v1.

[15] Dan-di Wu, *A brief introduction to the strong CP problem*, 1991. https://www.osti.gov/biblio/6260191.

[16] https://cds.cern.ch/record/281332/files/9505231.pdf, 02.05.2022.

[17] Igor G. Irastorza, *An introduction to axions and their detection*, 2021. https://arxiv.org/pdf/2109.07376.pdf.

[18] Roberto D. Peccei, *The Strong CP Problem and Axions*, Lecture Notes in Physics 3-17, Springer Berlin Heidelberg 2008. https://arxiv.org/abs/hep-ph/0607268.

[19] D.S. Gorbunov, G. G. Raffelt, D. V. Semikoz, *Axion-Like Particles as Ultra High Energy Cosmic Rays?*, Physical Review D **64**, 9, American Physical Society 2001. https://arxiv.org/pdf/hep-ph/0103175.pdf.

[20] Georg Raffelt, Leo Stodolsky, *Mixing of the photon with low-mass particles*, Phys. Rev. D **37**, 5, American Physical Society 1988. https://journals.aps.org/prd/abstract/10.1103/PhysRevD.37.1237.

[21] I. Stern, *ADMX Status*, 2016. https://www.researchgate.net/publication/311925873_ADMX_Status.

[22] Theopisti Dafni, Javier Galan, *Digging into Axion Physics with (Baby)IAXO*,Universe **8**, 37, 2022. https://doi.org/10.3390/universe8010037.

[23] https://chandra.harvard.edu/edu/formal/variable_stars/bg_info.html, 08.06.2022.

[24] Igor G. Irastorza, Javier Redondo, *New experimental approaches in the search for axion-like particles*, Progress in Particle and Nuclear Physics **102**, Elsevier BV 2018. https://arxiv.org/pdf/1801.08127.pdf.

[25] Peter Schneider, *Einführung in die Extragalaktische Astronomie und Kosmologie*, Springer-Verlag 2008.

[26] C. Csáki, N.Kaloper, J. Terning *Dimming Supernovae without Cosmic Acceleration*, Physical Review Letters **88**, 16, American Physical Society 2002. https://journals.aps.org/prl/pdf/10.1103/PhysRevLett.88.161302.

[27] Christopher Eckner, Francesca Calore, *First constraints on axion-like particles from Galactic sub-PeV gamma rays*, arXiv 2022. https://arxiv.org/abs/2204.12487.

[28] Berta Beltran *Search for solar axions: the CAST experiment at CERN*, arXiv 2005. https://arxiv.org/abs/hep-ex/0507007v1.

[29] N. W. Evans, C. A. J. O'Hare, C McCabe, *SHM^{++}: A Refinement of the Standard Halo Model for Dark Matter Searches in Light of the Gaia Sausage* 2018. https://arxiv.org/pdf/1810.11468.pdf.

[30] J. A. Grifols and E. Massó and R. Toldrà *Gamma Rays from SN1987A due to Pseudoscalar Conversion*, Physical Review Letters **77** 12, American Physical Society (APS) 1996. https://arxiv.org/abs/astro-ph/9606028.

[31] https://www.icrr.u-tokyo.ac.jp/em/index.html, 27.04.2022.

[32] https://www.hawc-observatory.org/observatory/, 27.04.2022.

[33] Maurizio Giannotti, *ALP hints from cooling anomalies*, arXiv 2015. https://arxiv.org/abs/1508.07576.

[34] Ciaran O'Hare, *cajohare/AxionLimits: AxionLimits*, Zenodo 2020. https://cajohare.github.io/AxionLimits/.

[35] Manuel Meyer, James Davies, Julian Kuhlmann, *gammaALPs: An open-source python package for computing photon-axion-like-particle oscillations in astrophysical environments*, Sissa Medialab 2021. https://arxiv.org/abs/2108.02061.

[36] Manuel Meyer, James Davies, Julian Kuhlmann, *gammaALPs*, 2017. https://github.com/me-manu/gammaALPs.

[37] M. Meyer, D. Montanino, J. Conrad, *On detecting oscillations of gamma rays into axion-like particles in turbulent and coherent magnetic fields*, Journal of Cosmology and Astroparticle Physics **2014**, 09, IOP Publishing 2017. https://arxiv.org/pdf/1406.5972.pdf.

[38] P.A. Zyla et al. (Particle Data Group), *Physical constants (rev.)*, Prog. Theor. Exp. Phys. 2020, 083C01 (2020) and 2021 update. https://pdg.lbl.gov/2021/reviews/contents_sports.html.

[39] *Nicola Bassan, Alessandro Mirizzi, Marco Roncadelli*, Axion-like particle effects on the polarization of cosmic high-energy gamma sources, Journal of Cosmology and Astroparticle Physics **2010**, 5, IOP Publishing 2010. https://arxiv.org/abs/1001.5267v2

[40] Manuel Meyer et al., *gammaALPs*, 2021. https://gammaalps.readthedocs.io/en/latest/theory.html.

[41] Rainer Beck, Richard Wielebinski, *Magnetic Fields in Galaxies*, Planets, Stars and Stellar Systems, Springer Netherlands 2013. https://arxiv.org/abs/1302.5663.

[42] M. Meyer, J. Davies, J. Kuhlmann, *gammaALPs: An open-source python package for computing photon-axion-like-particle oscillations in astrophysical environments*, Proceedings of 37th International Cosmic Ray Conference — PoS(ICRC2021), Sissa Medialab 2021. https://arxiv.org/pdf/2108.02061.pdf.

[43] C. Csáki, N.Kaloper, J. Terning *Effects of the Intergalactic Plasma on Supernova Dimming via Photon-Axion Oscillations*, Physics Letters B **535**, 1-4, 2002. https://arxiv.org/pdf/hep-ph/0112212.pdf.

[44] M. Fairbairn, T. Rashba, S. Troitsky, *Photon-axion mixing and ultra-high energy cosmic rays from BL Lac type objects: Shining light through the Universe*, Physical Review D **84**, 12, American Physical Society 2011. https://arxiv.org/pdf/0901.4085.pdf.

[45] A. Dobrynina, A. Kartavtsev, G. Raffelt, *Photon-photon dispersion of TeV gamma rays and its role for photon-ALP conversion*, Physical Review D **95**, 10, American Physical Society 2017. https://arxiv.org/pdf/1412.4777.pdf.

[46] A. Mirizzi, G. G. Raffelt, P. D. Serpico, *Photon-Axion Conversion in Intergalactic Magnetic Fields and Cosmological Consequences*, Axions, Springer Berlin Heidelberg 2006. https://arxiv.org/pdf/astro-ph/0607415v1.pdf.

[47] E. Masaki, A. Aoki, J. Soda, *Photon-axion conversion, magnetic field configuration, and polarization of photons*, Physical Review D **96**, 4, American Physical Society 2017. https://arxiv.org/pdf/1702.08843.pdf.

[48] S. K. Ocker, J. M. Cordes, S. Chatterjee, *Electron Density Structure of the Local Galactic Disk*, The Astrophysical Journal **897**, 2, American Astronomical Society 2020. https://arxiv.org/pdf/2004.11921.pdf.

[49] C. Csáki, N. Kaloper, J. Terning, *Effects of the intergalactic plasma on supernova dimming via photon–axion oscillations*, Physics Letters B **535**, 1-4, Elsevier BV 2002. https://arxiv.org/pdf/hep-ph/0112212.pdf.

[50] Federica Govoni, Luigina Feretti, *Magnetic Field in Clusters of Galaxies*, International Journal of Modern Physics D **13**, 08, World Scientific Pub Co Pte Lt 2004. https://arxiv.org/pdf/astro-ph/0410182.pdf.

[51] Alexander M. Beck et al., *On the magnetic fields in voids*, Monthly Notices of the Royal Astronomical Society: Letters **429**, 1, Oxford University Press 2012. https://arxiv.org/pdf/1210.8360.pdf.

[52] Christopher S. Reynolds et al., *Astrophysical Limits on Very Light Axion-like Particles from Chandra Grating Spectroscopy of NGC 1275*, The Astrophysical Journal **890**, 1, American Astronomical Society 2020. https://arxiv.org/pdf/1907.05475.pdf.

[53] B. B. Zhang et al., *A peculiar low-luminosity short gamma-ray burst from a double neutron star merger progenitor*, Nat Commun **9**, 447, 2018. https://doi.org/10.1038/s41467-018-02847-3.

[54] http://www.messier.seds.org/more/m031_sAnd.html, 29.06.2022.

[55] Roger A. Chevalier and Philip C. Plait, *The Nature of S Andromedae (SN 1885A)*, The Astrophysical Journal Letters **331**, 1988. https://ui.adsabs.harvard.edu/abs/1988ApJ...331L.109C/abstract.

[56] B. P. Abbott et al., *GWTC-1: A Gravitational-Wave Transient Catalog of Compact Binary Mergers Observed by LIGO and Virgo during the First and Second Observing Runs*, Physical Review X **9**, 3, American Physical Society 2019. https://arxiv.org/abs/1811.12907.

[57] Maria Petropoulou et al., *Multi-epoch Modeling of TXS 0506+056 and Implications for Long-term High-energy Neutrino Emission*, The Astrophysical Journal **891**, 2, The American Astronomical Society 2020. https://iopscience.iop.org/article/10.3847/1538-4357/ab76d0.

[58] J. S. Bloom, S. G. Djorgovski, S. R. Kulkarni, *The Redshift and the Ordinary Host Galaxy of GRB 970228*, The Astrophysical Journal **554**, 2, American Astronomical Society 2001. https://arxiv.org/abs/astro-ph/0007244v1.

[59] George Djorgovski et al., *GRB 970228: redshift and properties of the host galaxy.*, GRB Coordinates Network **289**, 1999. https://gcn.gsfc.nasa.gov/gcn/gcn3/289.gcn3.

[60] M. Arabsalmani et al., *The host galaxy of GRB 980425/SN1998bw: a collisional ring galaxy*, Monthly Notices of the Royal Astronomical Society **485**, 4, Oxford University Press 2019. https://arxiv.org/abs/1903.00485v1.

[61] S. R. Kulkarni et al., *The gamma-ray burst of 980425 and its association with the extraordinary radio emission from a most unusual supernova*, arXiv e-prints 1998. https://ui.adsabs.harvard.edu/abs/1998astro.ph..7001K/abstract.

[62] Kate Scholberg, *Supernova Neutrino Detection*, Annual Review of Nuclear and Particle Science **62**, 1, Annual Reviews 2012. https://arxiv.org/abs/1205.6003v1.

[63] Yudai Suwa et al., *Observing Supernova Neutrino Light Curves with Super-Kamiokande: Expected Event Number over 10 s*, The Astrophysical Journal **881**, 2, American Astronomical Society 2019. https://arxiv.org/abs/1904.09996v2.

[64] A. Albert et al., *Search for High-energy Neutrinos from Binary Neutron Star Merger GW170817 with ANTARES, IceCube, and the Pierre Auger Observatory*, The Astrophysical Journal **850**, 2, American Astronomical Society 2017. https://arxiv.org/abs/1710.05839.

Eigenständigkeitserklärung

Hiermit erkläre ich, dass ich die vorliegende Arbeit selbstständig verfasst und keine anderen als die angegebenen Quellen und Hilfsmittel benutzt habe.

Alle sinngemäß und wörtlich übernommenen Textstellen aus fremden Quellen wurden kenntlich gemacht.

Name: _____

Datum: _____